# A Novel 3D GBSM and BDCM for 6G mmWave Massive MIMO ISAC Systems

Runruo Yang, *Student Member, IEEE*, Cheng-Xiang Wang, *Fellow, IEEE*, Rui Feng, *Member, IEEE*, Jie Huang, *Member, IEEE*, Yunfei Chen, *Senior Member, IEEE*, and El-Hadi M. Aggoune, L*ife Senior Member, IEEE*

***Abstract*—In this paper, a novel three-dimensional (3D) geometry-based stochastic model (GBSM) and a beam domain channel model (BDCM) for sixth-generation (6G) millimeter wave (mmWave) massive multiple-input multiple-output (MIMO) integrated sensing and communication (ISAC) systems are proposed. The spherical wavefront and space-time-frequency non-stationarity introduced by massive MIMO, movements of the user and clusters, and large bandwidth of mmWave communications are incorporated. The shared clusters between the sensing channel and communication channel caused by the scattering characteristics are also considered. Based on the proposed channel model, important statistical properties are derived and simulated, including the space-time-frequency correlation function (STF-CF), root mean square (RMS) beam spread, RMS delay spread, RMS Doppler spread, coherence time, and channel capacity. By comparing the statistical properties of the sensing channel and the communication channel, it is found that the sensing channel exhibits more significant temporal non-stationarity. Moreover, the distribution of clusters for the sensing channel and communication channel shows significant difference, which is confirmed by the simulation results of RMS beam spread and RMS delay spread.**

***Index Terms*—Integrated sensing and communication, mmWave, massive MIMO, GBSM, BDCM.**

## I. Introduction

With the advance of wireless communication technologies, the emerging sixth-generation (6G) wireless communication system has attracted widespread research interests. The goal of 6G is to achieve global coverage, all spectra, full applications, all senses, all digital, and strong security [1], [2]. Integrated sensing and communication (ISAC) is an important emerging application scenario for 6G [3]. It refers to the sharing of hardware and spectrum resources for sensing and communication to achieve high-precision sensing and high-speed communication in one system [4], [5]. The massive multiple-input multiple-output (MIMO) and millimeter wave (mmWave) technologies provide good support for such application. Massive MIMO utilizes large-scale arrays to narrow the beamwidth of the beam, which is beneficial for high angular resolution sensing [6], [7] and for high data rate communications [8], [9]. Furthermore, mmWave can provide a larger bandwidth than sub-6 GHz frequency bands, ensuring a higher delay resolution for the sensing system and a higher data rate for communication systems [4], [10], [11].

At present, a large number of research has been conducted on signal processing [12]–[15], hardware design [14]–[16], and system performance evaluation [17], [18] for ISAC systems. For example, in [12] and [13], beamforming methods for ISAC systems were proposed, and the proposed methods were evaluated assuming the Rayleigh fading channel and Saleh-Valenzuela channel. A mmWave massive MIMO processing framework of ISAC was proposed in [14], and two uncorrelated time-varying channel models were used to represent the sensing and communication channels. The multibeam framework of the ISAC system based on a steerable analogue antenna array was proposed in [15], and the sensing and communication channels were modeled as time-varying channels. Authors in [16] studied the differences in beamforming and precoding under different hardware constraints and channel characteristics in mmWave MIMO system. Authors in [17] proposed a discrete Fourier transform spread orthogonal frequency division multiplexing system for the terahertz ISAC system, and two independent channel models were used to represent the sensing and communication channels. A method for evaluating the target detection performance of the uplink ISAC system was proposed in [18], and line-of-sight (LoS) path and non-LoS (NLoS) paths were used to model communication and sensing channels, respectively. However, these studies have not thoroughly investigated the channel properties. Moreover, sensing and communication channels have assumed independent channels.

Channel modeling is essential for fundamental theory, system design and construction, and performance analysis. There are already many studies on massive MIMO and mmWave channels in the literature. For massive MIMO channels, due to the large aperture of the array, the visible clusters are

This work was supported by the National Natural Science Foundation of China (NSFC) under Grants 62394290, 62394291, and 62301366, the Fundamental Research Funds for the Central Universities under Grant 2242022k60006, the Key Technologies R&D Program of Jiangsu (Prospective and Key Technologies for Industry) under Grants BE2022067, BE2022067-1, and BE2022067-2, the Research Fund of National Mobile Communications Research Laboratory, Southeast University, under Grant 2025A05, and AIST Research Center at the University of Tabuk of Saudi Arabia under Grant 1444-154. (*Corresponding Authors: Cheng-Xiang Wang and Rui Feng.*)

R. Yang, C.-X. Wang, and J. Huang are with the National Mobile Communications Research Laboratory, School of Information Science and Engineering, Southeast University, Nanjing 211189, China, and also with the Pervasive Communication Research Center, Purple Mountain Laboratories, Nanjing 211111, China (email: {yang_rr, chxwang, j_huang}@seu.edu.cn).

R. Feng is with the Pervasive Communication Research Center, Purple Mountain Laboratories, Nanjing 211111, China (e-mail: fengrui@pmlabs.com.cn).

Y. Chen is with the Department of Engineering, University of Durham, Durham, DH1 3LE, U.K. (e-mail: Yunfei.Chen@durham.ac.uk).

H. Aggoune is with the Sensor Networks and Cellular Systems Research Center, University of Tabuk, Tabuk 47315/4031, Saudi Arabia (email: haggoune@ut.edu.sa).

different among different antennas, leading to spatial non-stationarity. The spatial non-stationarity can be captured using the visibility region (VR) [19]–[25] or birth-death process [26]–[31] of clusters. In addition, if the array aperture is large enough, the distance between the array and the user or cluster will be smaller than the Rayleigh distance, and the far-field assumption will not be satisfied. Therefore, the spherical wavefront needs to be taken into account under the near-field condition [22], [26]–[31]. In [19]–[22], [26]–[29], massive MIMO geometry-based stochastic models (GBSMs) were proposed for different scenarios. In [23], [30], [31], non-stationary massive MIMO beam domain channel models (BDCMs) were proposed. These BDCMs are modeled using the steering vectors of uniform planar arrays (UPAs) with planar wavefront [23], uniform circular arrays [30], and uniform linear arrays [31], respectively. A general form of the steering vector for large-scale UPAs considering both spherical and planar wavefronts is still missing. For mmWave channels, due to the large bandwidth of mmWave, the channel is non-stationary in the frequency domain. It can be depicted by the birth-death process of clusters. Besides, the delay resolution of paths increases as well. The 3GPP TR 38.901 document [32] provided the channel modeling framework for 0.5–100 GHz frequency bands and clarified specific parameter modeling methods. Furthermore, in order to accurately capture the characteristics of mmWave channel, numerous mmWave non-stationary GBSMs were proposed for different scenarios in [33]–[38]. However, most of these channel models focus on the communication channel, while in-depth research on the sensing channel is limited. The sensing channel, as an essential part of the ISAC channel, has a significantly different composition from the communication channel. For example, since the transmitter (Tx) and receiver (Rx) of the sensing channel are co-located, the sensing channel is composed of a round-trip signal that suffers from double multipath fading. In practical sensing applications, LoS propagation is typically relied upon between the sensing base station (BS) and targets for achieving target localization using echoes. However, the communication channel is mainly composed of NLoS multi-paths in most scenarios, due to the long distance between communication Tx and Rx. Moreover, the round-trip of the sensing channel inevitably leads to different channel characteristics from those of the communication channel, notably including more significant time variety. However, there is still a lack of in-depth and comprehensive research on the differences between communication and sensing channel characteristics. Additionally, it remains a challenge to examine the effect of mmWave or massive MIMO on sensing channels. Therefore, there is an urgent need to model and conduct a comprehensive analysis of the sensing channel for mmWave massive MIMO ISAC systems. Furthermore, it is also crucial to find the difference and correlation between the sensing channel and communication channel for mmWave massive MIMO ISAC systems.

Due to being in the same physical environment, sensing and communication channels may be correlated with each other. In order to make further insight into the correlation between the sensing channel and communication channel, the measurements were introduced in [39] and [40]. The results indicated that there was the sharing characteristic between sensing and communication channels. Considering the correlation between sensing and communication, an ISAC GBSM at sub-6 GHz was proposed in our previous work [41], and the scattering characteristics were introduced in the channel model. An ISAC channel model framework based on 3GPP TR 38.901 was proposed in [42]. The sensing channel model framework and sensing clusters were proposed to compensate for the shortcoming of the 3GPP channel model that does not support the model of sensing channel. However, the mmWave and massive MIMO, which are key technologies for ISAC systems, were not considered in the existing ISAC channel models. Thus, it is necessary to model sensing and communication channels in the ISAC channel. Due to the different structures of these two parts, there will be differences in their parameters. Moreover, the relations between sensing and communication channels need to be fully considered in the ISAC channel model. Accurately modeling the ISAC channel model, while taking into consideration both sensing and communication, continues to pose a significant challenge. Additionally, the impact of mmWave and massive MIMO technologies on both parts also need to be taken into account. However, there is currently no channel model proposed that fully considers the above aspects and can support mmWave massive MIMO ISAC systems.

To fill the gaps mentioned above, we first propose a novel 3D non-stationary mmWave massive MIMO ISAC GBSM to extend our previous research [41]. Compared with the GBSM in [41], large-scale aperture arrays and mmWave frequency bands are introduced in the proposed GBSM. The space-time-frequency non-stationarity, spherical wavefront effect, and correlation between sensing and communication channels are considered. Then, an ISAC BDCM is proposed based on the GBSM. The main novelties and contributions of this paper are as follows.

1) A novel 6G 3D non-stationary mmWave massive MIMO ISAC GBSM and BDCM are proposed. The mono-static sensing channel and the communication channel are modeled. Because of the scattering characteristics of clusters, the shared clusters between sensing and communication channels are considered. This leads to the correlation between sensing and communication channels.
2) The spherical wavefront and the space-time-frequency non-stationarity introduced by massive MIMO, movements of the user and clusters, and mmWave, respectively, are incorporated in the channel model. To capture the spherical wavefront effect caused by large array aperture, a general form of the steering vector is proposed, which is applicable to both spherical wavefront and plane wavefront.
3) Key statistical properties of the proposed ISAC channel model, including space-time-frequency correlation functions (STF-CFs), root mean square (RMS) beam spread, RMS delay spread, RMS Doppler spread, coherence time, and channel capacity, are derived and simulated. Detailed comparisons of statistical properties between the

sensing GBSM, sensing BDCM, communication GBSM, and communication BDCM are conducted taking into account the correlation between sensing and communication channels.

The remainder of this paper is outlined as follows. The novel 6G 3D non-stationary mmWave massive MIMO ISAC GBSM and BDCM are proposed in Section II and Section III, respectively. Section IV derives some key statistical properties of the ISAC GBSM and BDCM. In Section V, results and analysis of channel statistical properties are presented. Finally, conclusions are drawn in Section VI.

## II. A Novel 3D Non-stationary mmWave Massive MIMO ISAC GBSM

The diagram of the ISAC system is shown in Fig. 1 (a), which includes the mono-static sensing system and the communication system. The BS is equipped with one transmitting array and one receiving array to form a mono-static sensing system. Both arrays are uniform planar arrays (UPAs). The transmitting UPA is used to transmit the ISAC signal, which is integrated with communication and sensing functions. The receiving UPA can receive the sensing echo signal. The number of antennas in the horizontal and vertical directions of the transmitting (receiving) UPA are $P_{\mathrm{h}}$ ($Q_{\mathrm{h}}^{\mathrm{s}}$) and $P_{\mathrm{v}}$ ($Q_{\mathrm{v}}^{\mathrm{s}}$), respectively. Therefore, $P = P_{\mathrm{h}} \times P_{\mathrm{v}}$ and $Q^{\mathrm{s}} = Q_{\mathrm{h}}^{\mathrm{s}} \times Q_{\mathrm{v}}^{\mathrm{s}}$ antennas are in the transmitting and receiving UPAs, respectively. At the communication user (UE), there is a receiving UPA with $Q^{\mathrm{c}} = Q_{\mathrm{h}}^{\mathrm{c}} \times Q_{\mathrm{v}}^{\mathrm{c}}$ antennas, where $Q_{\mathrm{h/v}}^{\mathrm{c}}$ is the number of antennas in the horizontal/vertical direction. The spacing between two adjacent elements of the transmitting and receiving UPAs are $\Delta_{\mathrm{T}}$ and $\Delta_{\mathrm{R}}$, respectively. We set $\Delta_{\mathrm{T}} = \Delta_{\mathrm{R}} = \frac{\lambda}{2}$, where $\lambda$ is the wavelength. The speed of UE is $v_{\mathrm{R}}(t)$, and the movement direction is $\alpha_{\mathrm{R}}(t)$. For clarity, we summarize the main parameters of the channel model in Table I.

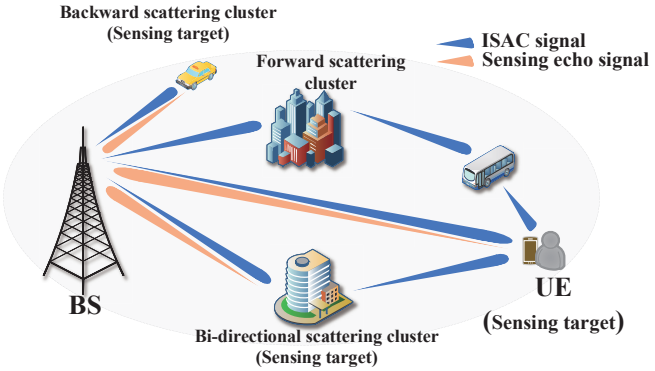


(a) The ISAC system

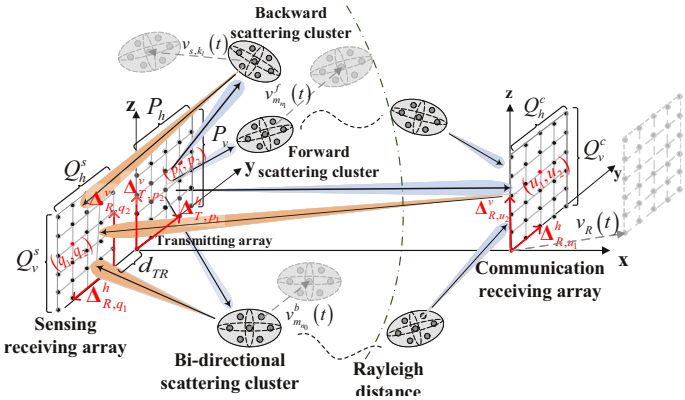


(b) The ISAC channel model

Fig. 1. The diagrams of (a) the ISAC system and (b) the ISAC channel model.

The scattering characteristic of the object is an important factor that should be considered in the sensing channel. There are two types of object scattering, i.e., the forward scattering and the backward scattering [43]–[45]. When the angle between the scattering direction and the incident direction is less than $90°$, it is the forward scattering. Otherwise, it is the backward scattering. For the sensing channel, the signal is transmitted by the BS, and if the signal reaches the target, the target will backscatter the signal to the sensing Rx at the BS, as shown by the orange arrows in Fig.1 (b). These backscattered echo paths constitute the sensing channel. However, the communication channel is composed of forward transmission multipath, as shown by the blue arrows in Fig.1 (b), which means it does not have a backward scattering echo path. Considering the scattering characteristics of clusters, the communication channel is divided into LoS, forward scattering, and bi-directional scattering paths, which are explained in detail in subsection B. Due to the significant difference between the sensing channel and communication channel, the modeling process of the sensing channel and communication channel is elaborated on separately. The GBSM in the antenna domain is the foundation of BDCM. Therefore, we first model the GBSM for the ISAC system and then obtain the BDCM from the GBSM.

### A. Sensing Channel Modeling

The mono-static sensing channel is composed of single-bounce backward scattering cluster paths, where these clusters are the targets of the mono-static sensing system, as shown in Fig. 1 (a). The paths with multi-bounce clusters are classified as clutters, which are not considered here. The total number of clusters in the sensing channel is $L(t,f)$, and there are $K_l$ scatterers within the $l$th ($l = 1, \ldots, L(t,f)$) cluster. The distance between the first transmitting (receiving) antenna and the $k$th scatterer is $d_{\mathrm{T}}^{\mathrm{s},k_l}(t)$ ($d_{\mathrm{R}}^{\mathrm{s},k_l}(t)$). The distance from the transmitting antenna in row $p_1$ ($p_1 = 1, \ldots, P_{\mathrm{h}}$) and column $p_2$ ($p_2 = 1, \ldots, P_{\mathrm{v}}$) to the $k$th ($k = 1, \ldots, K_l$) scatterer is $d_{\mathrm{T},p_1,p_2}^{\mathrm{s},k_l}(t)$. The distance between the receiving antenna in row $q_1$ ($q_1 = 1, \ldots, Q_{\mathrm{h}}^{\mathrm{s}}$) and column $q_2$ ($q_2 = 1, \ldots, Q_{\mathrm{v}}^{\mathrm{s}}$) and the $k$th scatterer is $d_{\mathrm{R},q_1,q_2}^{\mathrm{s},k_l}(t)$. The azimuth angle of departure/arrival (AOD/AOA) and the zenith angle of departure/arrival (ZOD/ZOA) from the transmitting/receiving array to the $k$th scatterer are $\theta_{\mathrm{T/R},k_l}^{\mathrm{s,az}}(t)$ and $\theta_{\mathrm{T/R},k_l}^{\mathrm{s,el}}(t)$, respectively. We assume that the scatterer is moving. The speed and angle of the $k$th scatterer are $v_{\mathrm{s},k_l}(t)$ and $\alpha_{\mathrm{s},k_l}(t)$, respectively.

The sensing channel transfer function (CTF) between the transmitting antenna in row $p_1$ and column $p_2$ and the receiv-

TABLE I. DEFINITIONS OF MAIN PARAMETERS OF THE ISAC CHANNEL.

| Parameters | Definitions |
|---|---|
| $P_{\mathrm{h}/v}$, $Q_{\mathrm{h}/v}^{\mathrm{s}(c)}$ | The number of antennas of transmitting and sensing (communication) receiving UPAs in horizontal/vertical direction, respectively |
| $\Delta_{\mathrm{T/R}}$ | Antenna spacings of transmitting/receiving UPA |
| $L\left(t,f\right)$, $K_l$ | The number of clusters of the sensing channel and the number of scatterers in the cluster |
| $N_1\left(t,f\right)/N_0\left(t,f\right)$, $M_{n_1}/M_{n_0}$ | The number of clusters and the number of scatterers within the cluster of forward/backward scattering component, respectively |
| $d_{\mathrm{L}}\left(t\right)$ | The distance between the transmitting array of BS and UE |
| $d_{\mathrm{T(R)}}^{\mathrm{s},k_l}\left(t\right)$ | The distance between the first transmitting (receiving) antenna and the $k$th scatterer of the sensing channel |
| $d_{\mathrm{T},p_1,p_2}^{\mathrm{s},k_l}\left(t\right)$, $d_{\mathrm{R},q_1,q_2}^{\mathrm{s},k_l}\left(t\right)$ | The distance between the transmitting antenna in $p_1$ row and $p_2$ column (receiving in $q_1$ row and $q_2$ column) antenna and the $k$th scatterer of the sensing channel, respectively |
| $d_{\mathrm{T(R)}}^{\mathrm{c},m_{n_1}}\left(t\right)$, $d_{\mathrm{T(R)}}^{\mathrm{c},m_{n_0}}\left(t\right)$ | The distance between the first transmitting (receiving) antenna and the $m$th scatterer of forward and bi-directional scattering part of the communication channel, respectively |
| $d_{\mathrm{T},p_1,p_2}^{\mathrm{c},m_{n_1}}\left(t\right)/d_{\mathrm{T},p_1,p_2}^{\mathrm{c},m_{n_0}}\left(t\right)$ | The distance between the transmitting antenna in $p_1$ row and $p_2$ column and the $m$th scatterer of forward/bi-directional scattering part of the communication channel, respectively |
| $d_{\mathrm{R},u_1,u_2}^{\mathrm{c},m_{n_1}}\left(t\right)/d_{\mathrm{R},u_1,u_2}^{\mathrm{c},m_{n_0}}\left(t\right)$ | The distance between the receiving antenna in $u_1$ row and $u_2$ column and the $m$th scatterer of forward/bi-directional scattering parts of the communication channel |
| $\theta_{\mathrm{T/R},k_l}^{\mathrm{s,az}}\left(t\right)$, $\theta_{\mathrm{T/R},k_l}^{\mathrm{s,el}}\left(t\right)$ | AOD/AOA and ZOD/ZOA of the $k$th path within the $l$th cluster of the sensing channel, respectively |
| $\phi_{\mathrm{T/R}}^{\mathrm{L,az}}\left(t\right)$, $\phi_{\mathrm{T/R}}^{\mathrm{L,el}}\left(t\right)$ | AOD/AOA and ZOD/ZOA of LoS path of the communication channel, respectively |
| $\phi_{\mathrm{T/R},m_{n_1}}^{\mathrm{f,az}}\left(t\right)$, $\phi_{\mathrm{T/R},m_{n_1}}^{\mathrm{f,el}}\left(t\right)$ | AOD/AOA and ZOD/ZOA of the $m$th path within the $n_1$th cluster of the forward scattering part of the communication channel, respectively |
| $\phi_{\mathrm{T/R},m_{n_0}}^{\mathrm{b,az}}\left(t\right)$, $\phi_{\mathrm{T/R},m_{n_0}}^{\mathrm{b,el}}\left(t\right)$ | AOD/AOA and ZOD/ZOA of the $m$th path within the $n_0$th cluster of the bi-directional scattering part of the communication channel, respectively |
| $v_{\mathrm{R}}\left(t\right)$, $\alpha_{\mathrm{R}}\left(t\right)$ | The movement speed and direction of UE, respectively |
| $v_{\mathrm{s},k_l}\left(t\right)$, $\alpha_{\mathrm{s},k_l}\left(t\right)$ | The movement speed and direction of the $k$th scatterer of the sensing channel, respectively |
| $v_{m_{n_1}}^{\mathrm{f}}\left(t\right)/v_{m_{n_0}}^{\mathrm{b}}\left(t\right)$, $\alpha_{m_{n_1}}^{\mathrm{f}}\left(t\right)/\alpha_{m_{n_0}}^{\mathrm{b}}\left(t\right)$ | The movement speed and direction of the $m$th scatterer of forward/bi-directional scattering parts of the communication channel, respectively |

ing antenna in row $q_1$ and column $q_2$ can be represented as

$$\begin{aligned} &h_{p_1,p_2,q_1,q_2}^{\mathrm{s}}\left(t,f\right) \\ &=\sum_{l=1}^{L(t,f)}\sum_{k=1}^{K_l}\beta_{\mathrm{s},k_l}e^{j\left[2\pi\left(\omega_{\mathrm{s},k_l}\left(t\right)t-f\tau_{\mathrm{s},k_l}\left(t\right)\right)+\Phi_{\mathrm{s},k_l}\right]}\cdot e^{j\frac{2\pi}{\lambda}\Delta d_{k_l}^{\mathrm{SW}}\left(t\right)} \end{aligned} \tag{1}$$

where $\beta_{\mathrm{s},k_l}$ is the complex channel gain, which is determined by the radar equation [46], $\omega_{\mathrm{s},k_l}\left(t\right)$ is Doppler shift, $\tau_{\mathrm{s},k_l}\left(t\right)=\left(d_{\mathrm{T},p_1,p_2}^{\mathrm{s},k_l}\left(t\right)+d_{\mathrm{R},q_1,q_2}^{\mathrm{s},k_l}\left(t\right)\right)/\mathrm{c}$ is the delay, c is the speed of light, $\Phi_{\mathrm{s},k_l}$ is the random phase of the sensing path, and $\Delta d_{k_l}^{\mathrm{SW}}\left(t\right)$ is the distance difference caused by antenna spacing. The distance can be expressed as $d_{\mathrm{T},p_1,p_2}^{\mathrm{s},k_l}\left(t\right)=\left|\mathbf{d}_{\mathrm{T},p_1,p_2}^{\mathrm{s},k_l}\left(t\right)\right|$, where $\mathbf{d}_{\mathrm{T},p_1,p_2}^{\mathrm{s},k_l}\left(t\right)$ is the distance vector from the transmitting antenna on the $p_1$th row and $p_2$th column to the $k$th scatterer. The distance vector can be modeled as

$$\mathbf{d}_{\mathrm{T},p_1,p_2}^{\mathrm{s},k_l}\left(t\right)=\mathbf{d}_{\mathrm{T}}^{\mathrm{s},k_l}\left(t\right)-\left(\mathbf{\Delta}_{\mathrm{T},p1}^{\mathrm{h}}+\mathbf{\Delta}_{\mathrm{T},p2}^{\mathrm{v}}\right). \tag{2}$$

Symbol $\mathbf{\Delta}_{\mathrm{T},p_1}^{\mathrm{h}}=[0,p_1-1,0]\cdot\Delta_{\mathrm{T}}$ ($\mathbf{\Delta}_{\mathrm{T},p_2}^{\mathrm{v}}=[0,0,p_2-1]\cdot\Delta_{\mathrm{T}}$) represents the distance vector from the first antenna to the $p_1$th row ($p_2$th column) antenna of the transmitting array in the horizontal (vertical) direction, as shown in Fig. 1 (b). The distance vector from the first antenna to the $k$th scatterer is

$$\begin{aligned} \mathbf{d}_{\mathrm{T}}^{\mathrm{s},k_l}\left(t\right)=d_{\mathrm{T}}^{\mathrm{s},k_l}\left(t\right)\Big[&\cos\left(\theta_{\mathrm{T},k_l}^{\mathrm{s,el}}\left(t\right)\right)\cos\left(\theta_{\mathrm{T},k_l}^{\mathrm{s,az}}\left(t\right)\right), \\ &\cos\left(\theta_{\mathrm{T},k_l}^{\mathrm{s,el}}\left(t\right)\right)\sin\left(\theta_{\mathrm{T},k_l}^{\mathrm{s,az}}\left(t\right)\right),\sin\left(\theta_{\mathrm{T},k_l}^{\mathrm{s,el}}\left(t\right)\right)\Big]. \end{aligned} \tag{3}$$

The distance $d_{\mathrm{T}}^{\mathrm{s},k_l}\left(t\right)$, AOD $\theta_{\mathrm{T},k_l}^{\mathrm{s,az}}\left(t\right)$, and ZOD $\theta_{\mathrm{T},k_l}^{\mathrm{s,el}}\left(t\right)$ can be determined by ellipsoid Gaussian scattering distribution [47]. The receiving distance vector is

$$\mathbf{d}_{\mathrm{R},q_1,q_2}^{\mathrm{s},k_l}\left(t\right)=\mathbf{d}_{\mathrm{R}}^{\mathrm{s},k_l}\left(t\right)-\left(\mathbf{\Delta}_{\mathrm{R},q_1}^{\mathrm{h}}+\mathbf{\Delta}_{\mathrm{R},q_2}^{\mathrm{v}}\right) \tag{4}$$

where antenna spacing vectors in the horizontal and vertical directions are $\mathbf{\Delta}_{\mathrm{R},q_1}^{\mathrm{h}}=[0,q_1-1,0]\cdot\Delta_{\mathrm{R}}$, $\mathbf{\Delta}_{\mathrm{R},q_2}^{\mathrm{v}}=[0,0,q_2-1]\cdot\Delta_{\mathrm{R}}$, respectively. Since the transmitting and receiving UPAs of sensing are arranged side by side in the $y-z$ plane, as shown in Fig. 1 (b), the relationship between two distance vectors $\mathbf{d}_{\mathrm{T}}^{\mathrm{s},k_l}\left(t\right)$ and $\mathbf{d}_{\mathrm{R}}^{\mathrm{s},k_l}\left(t\right)$ can be written as $\mathbf{d}_{\mathrm{R}}^{\mathrm{s},k_l}\left(t\right)=\mathbf{d}_{\mathrm{T}}^{\mathrm{s},k_l}\left(t\right)-\Delta\mathbf{d}_{\mathrm{TR}}$, where $\Delta\mathbf{d}_{\mathrm{TR}}=[0,d_{\mathrm{TR}},0]$ represents the distance vector from the first transmitting antenna to the first receiving antenna at BS. The parameter $\Delta d_{k_l}^{\mathrm{SW}}\left(t\right)$ in (1) can be expressed as

$$\begin{aligned} \Delta d_{k_l}^{\mathrm{SW}}\left(t\right)=&\left[d_{\mathrm{T}}^{\mathrm{s},k_l}\left(t\right)-d_{\mathrm{T},p_1,1}^{\mathrm{s},k_l}\left(t\right)\right]+\left[d_{\mathrm{T}}^{\mathrm{s},k_l}\left(t\right)-d_{\mathrm{T},1,p_2}^{\mathrm{s},k_l}\left(t\right)\right] \\ &+\left[d_{\mathrm{R}}^{\mathrm{s},k_l}\left(t\right)-d_{\mathrm{R},q_1,1}^{\mathrm{s},k_l}\left(t\right)\right]+\left[d_{\mathrm{R}}^{\mathrm{s},k_l}\left(t\right)-d_{\mathrm{R},1,q_2}^{\mathrm{s},k_l}\left(t\right)\right]. \end{aligned} \tag{5}$$

The distances $d_{\mathrm{T},p_1,1}^{\mathrm{s},k_l}\left(t\right)$ and $d_{\mathrm{T},1,p_2}^{\mathrm{s},k_l}\left(t\right)$ can be calculated by (2). Using the Taylor series second-order approximation, $d_{\mathrm{T},p_1,1}^{\mathrm{s},k_l}\left(t\right)$ and $d_{\mathrm{T},1,p_2}^{\mathrm{s},k_l}\left(t\right)$ can be expressed as

$$\begin{aligned} &d_{\mathrm{T},p_1,1}^{\mathrm{s},k_l}\left(t\right) \\ &=d_{\mathrm{T}}^{\mathrm{s},k_l}\left(t\right)-\sin\left(\theta_{\mathrm{T},k_l}^{\mathrm{s,az}}\left(t\right)\right)\cos\left(\theta_{\mathrm{T},k_l}^{\mathrm{s,el}}\left(t\right)\right)\left(p_1-1\right)\Delta_{\mathrm{T}} \\ &+\frac{\left(p_1-1\right)^2{\Delta_{\mathrm{T}}}^2}{2d_{\mathrm{T}}^{\mathrm{s},k_l}\left(t\right)}\left(1-\sin^2\left(\theta_{\mathrm{T},k_l}^{\mathrm{s,az}}\left(t\right)\right)\cos^2\left(\theta_{\mathrm{T},k_l}^{\mathrm{s,el}}\left(t\right)\right)\right) \end{aligned} \tag{6}$$

and

$$\begin{aligned} d_{\mathrm{T},1,p_2}^{\mathrm{s},k_l}\left(t\right)=&d_{\mathrm{T}}^{\mathrm{s},k_l}\left(t\right)-\sin\left(\theta_{\mathrm{T},k_l}^{\mathrm{s,el}}\left(t\right)\right)\left(p_2-1\right)\Delta_{\mathrm{T}} \\ &+\frac{\left(p_2-1\right)^2{\Delta_{\mathrm{T}}}^2}{2d_{\mathrm{T}}^{\mathrm{s},k_l}\left(t\right)}\cos^2\left(\theta_{\mathrm{T},k_l}^{\mathrm{s,el}}\left(t\right)\right). \end{aligned} \tag{7}$$

Similarly, the distance $d_{\mathrm{R},q_1,1}^{\mathrm{s},k_l}\left(t\right)$ and $d_{\mathrm{R},1,q_2}^{\mathrm{s},k_l}\left(t\right)$ can be approximated using the Taylor second-order. By substituting $\Delta d_{k_l}^{\mathrm{SW}}\left(t\right)$ calculated using the above equations into the $e^{j\frac{2\pi}{\lambda}\Delta d_{k_l}^{\mathrm{SW}}\left(t\right)}$ of (1), the general phase change caused by antenna intervals can be obtained. If $d_{\mathrm{T}}^{\mathrm{s},k_l}\left(t\right)\gg\left(p_1-1\right)\Delta_{\mathrm{T}}$, $d_{\mathrm{T}}^{\mathrm{s},k_l}\left(t\right)\gg\left(p_2-1\right)\Delta_{\mathrm{T}}$, $d_{\mathrm{R}}^{\mathrm{s},k_l}\left(t\right)\gg\left(q_1-1\right)\Delta_{\mathrm{R}}$, and $d_{\mathrm{R}}^{\mathrm{s},k_l}\left(t\right)\gg\left(q_2-1\right)\Delta_{\mathrm{R}}$, the above formula will be simplified as the phase change under the planar wavefront

$$\mathbf{a}^{\mathrm{BS}}\left(\varphi\left(t\right),d\left(t\right)\right)=\left[1,...,e^{j\frac{2\pi}{\lambda}\left\{\varphi(t)(p_1-1)\Delta_{\mathrm{T}}+\frac{(p_1-1)^2{\Delta_{\mathrm{T}}}^2}{2d(t)}\left[1-\varphi^2(t)\right]\right\}},...\right]^{\mathrm{T}}_{p_1=1,...,P_{\mathrm{h}}} \tag{9}$$

$$\mathbf{b}^{\mathrm{BS}}\left(\varphi\left(t\right),d\left(t\right)\right)=\left[1,...,e^{j\frac{2\pi}{\lambda}\left\{\varphi(t)(p_2-1)\Delta_{\mathrm{T}}+\frac{(p_2-1)^2{\Delta_{\mathrm{T}}}^2}{2d(t)}\left[1-\varphi^2(t)\right]\right\}},...\right]^{\mathrm{T}}_{p_2=1,...,P_{\mathrm{v}}} \tag{10}$$

$$\mathbf{a}_{\mathrm{s}}^{\mathrm{R}}\left(\varphi\left(t\right),d\left(t\right)\right)=\left[1,...,e^{j\frac{2\pi}{\lambda}\left\{\varphi(t)(q_1-1)\Delta_{\mathrm{R}}+\frac{(q_1-1)^2{\Delta_{\mathrm{R}}}^2}{2d(t)}\left[1-\varphi^2(t)\right]\right\}},...\right]^{\mathrm{T}}_{q_1=1,...,Q_{\mathrm{h}}^{\mathrm{s}}} \tag{11}$$

$$\mathbf{b}_{\mathrm{s}}^{\mathrm{R}}\left(\varphi\left(t\right),d\left(t\right)\right)=\left[1,...,e^{j\frac{2\pi}{\lambda}\left\{\varphi(t)(q_2-1)\Delta_{\mathrm{R}}+\frac{(q_2-1)^2{\Delta_{\mathrm{R}}}^2}{2d(t)}\left[1-\varphi^2(t)\right]\right\}},...\right]^{\mathrm{T}}_{q_2=1,...,Q_{\mathrm{v}}^{\mathrm{s}}}. \tag{12}$$

assumption. For the convenience of representation, we set $\varphi_{\mathrm{T/R},k_l}^{\mathrm{h}}\left(t\right)=-\sin\left(\theta_{\mathrm{T/R},k_l}^{\mathrm{s,az}}\left(t\right)\right)\cos\left(\theta_{\mathrm{T/R},k_l}^{\mathrm{s,el}}\left(t\right)\right)\in[-1,1]$ and $\varphi_{\mathrm{T/R},k_l}^{\mathrm{v}}\left(t\right)=-\sin\left(\theta_{\mathrm{T/R},k_l}^{\mathrm{s,el}}\left(t\right)\right)\in[-1,1]$. The CTF can be represented as a matrix

$$\begin{aligned}\mathbf{H}^{\mathrm{s}}\left(t,f\right)=&\sum_{l=1}^{L(t,f)}\sum_{k=1}^{K_l}\beta_{\mathrm{s},k_l}e^{j\left[2\pi\left(\omega_{\mathrm{s},k_l}(t)t-f\tau_{\mathrm{s},k_l}(t)\right)+\Phi_{\mathrm{s},k_l}\right]}\\&\times\mathbf{V}_{\mathrm{s},k_l}\cdot\left(\mathbf{U}_{\mathrm{s},k_l}\right)^{\mathrm{T}}\end{aligned} \tag{8}$$

where $\left(\cdot\right)^{\mathrm{T}}$ represents transpose operation, and the response matrix of transmitting and receiving UPAs are $\mathbf{U}_{\mathrm{s},k_l}=\mathbf{b}^{\mathrm{BS}}\left(\varphi_{\mathrm{T},k_l}^{\mathrm{v}}\left(t\right),d_{\mathrm{T}}^{\mathrm{s},k_l}\left(t\right)\right)\otimes\mathbf{a}^{\mathrm{BS}}\left(\varphi_{\mathrm{T},k_l}^{\mathrm{h}}\left(t\right),d_{\mathrm{T}}^{\mathrm{s},k_l}\left(t\right)\right)\in\mathbf{C}^{P\times1}$ and $\mathbf{V}_{\mathrm{s},k_l}=\mathbf{b}_{\mathrm{s}}^{\mathrm{R}}\left(\varphi_{\mathrm{R},k_l}^{\mathrm{v}}\left(t\right),d_{\mathrm{R}}^{\mathrm{s},k_l}\left(t\right)\right)\otimes\mathbf{a}_{\mathrm{s}}^{\mathrm{R}}\left(\varphi_{\mathrm{R},k_l}^{\mathrm{h}}\left(t\right),d_{\mathrm{R}}^{\mathrm{s},k_l}\left(t\right)\right)\in\mathbf{C}^{Q^{\mathrm{s}}\times1}$, respectively, and $\otimes$ means the Kronecker product. Here, $\mathbf{a}^{\mathrm{BS}}\left(\varphi_{\mathrm{T},k_l}^{\mathrm{h}}\left(t\right),d_{\mathrm{T}}^{\mathrm{s},k_l}\left(t\right)\right)$ and $\mathbf{b}^{\mathrm{BS}}\left(\varphi_{\mathrm{T},k_l}^{\mathrm{v}}\left(t\right),d_{\mathrm{T}}^{\mathrm{s},k_l}\left(t\right)\right)$ are response vectors of the transmitting UPA in the azimuth direction $\varphi_{\mathrm{T},k_l}^{\mathrm{h}}\left(t\right)$ and elevation direction $\varphi_{\mathrm{T},k_l}^{\mathrm{v}}\left(t\right)$ with distance $d_{\mathrm{T}}^{\mathrm{s},k_l}\left(t\right)$, respectively. Similarly, $\mathbf{a}_{\mathrm{s}}^{\mathrm{R}}\left(\varphi_{\mathrm{R},k_l}^{\mathrm{h}}\left(t\right),d_{\mathrm{R}}^{\mathrm{s},k_l}\left(t\right)\right)$ and $\mathbf{b}_{\mathrm{s}}^{\mathrm{R}}\left(\varphi_{\mathrm{R},k_l}^{\mathrm{v}}\left(t\right),d_{\mathrm{R}}^{\mathrm{s},k_l}\left(t\right)\right)$ are response vectors of the sensing receiving UPA in the azimuth and elevation directions, respectively. Furthermore, the response vectors of BS and sensing Rx can be expressed as (9)–(12) written at the top of this page.

### *B. Communication Channel Modeling*

The communication channel consists of three parts, i.e., LoS, forward scattering, and bidirectional scattering paths, as shown in Fig. 1 (b). The bi-directional scattering path means that the first-bounce cluster of the path has both forward scattering and backward scattering characteristics. Therefore, the first-bounce clusters of the bi-directional scattering paths are shared in both sensing and communication channels. The parameters of these first-bounce clusters can be determined by the sensing channel, which has been illustrated in our previous work [41]. In addition, if the first-bounce clusters are unique to the communication channel, these paths are called forward scattering paths. The parameters of the forward scattering path can be generated by specific random process.

For the LoS path, the distance between the transmitting UPA and the UE is $d_{\mathrm{L}}\left(t\right)$. The AOD, AOA, ZOD, and ZOA are defined as $\phi_{\mathrm{T}}^{\mathrm{L,az}}\left(t\right)$, $\phi_{\mathrm{R}}^{\mathrm{L,az}}\left(t\right)$, $\phi_{\mathrm{T}}^{\mathrm{L,el}}\left(t\right)$, and $\phi_{\mathrm{R}}^{\mathrm{L,el}}\left(t\right)$, respectively. For the forward scattering paths, it can be assumed that there are $N_1\left(t,f\right)$ clusters, and the number of scatterers within the $n_1$th ($n_1$ = 1, …, $N_1\left(t,f\right)$) cluster is $M_{n_1}$. The $m$th scatterer moves in the $\alpha_{m_{n_1}}^{\mathrm{f}}\left(t\right)$ direction at velocity $v_{m_{n_1}}^{\mathrm{f}}\left(t\right)$. For the bi-directional scattering paths, the number of clusters is $N_0\left(t,f\right)$, and there are $M_{n_0}$ scatterers within the $n_0$th ($n_0$ = 1, …, $N_0\left(t,f\right)$) cluster. The motion velocity and direction of the $m$th scatterer in the $n_0$th cluster are $v_{m_{n_0}}^{\mathrm{b}}\left(t\right)$ and $\alpha_{m_{n_0}}^{\mathrm{b}}\left(t\right)$, respectively. The distance between the first transmitting antenna (first UE antenna) and the first-bounce (last-bounce) scatterer of forward/bi-directional scattering part via the $m$th path of the $n_1$th/$n_0$th cluster can be represented as $d_{\mathrm{T}}^{\mathrm{c},m_{n_1/0}}\left(t\right)$ ($d_{\mathrm{R}}^{\mathrm{c},m_{n_1/0}}\left(t\right)$). The distance from the $p_1$th row and $p_2$th column transmitting antenna ($u_1$th row and $u_2$th column UE receiving antenna) to the first-bounce (last-bounce) scatterer of forward/bi-directional scattering part via the $m$th path of the $n_1$th/$n_0$th cluster is $d_{\mathrm{T},p_1,p_2}^{\mathrm{c},m_{n_1/0}}\left(t\right)$ ($d_{\mathrm{R},u_1,u_2}^{\mathrm{c},m_{n_1/0}}\left(t\right)$). AOD and ZOD of the $m$th forward (bi-directional) scattering path can be defined as $\phi_{\mathrm{T},m_{n_1}}^{\mathrm{f,az}}\left(t\right)$ ($\phi_{\mathrm{T},m_{n_0}}^{\mathrm{b,az}}\left(t\right)$) and $\phi_{\mathrm{T},m_{n_1}}^{\mathrm{f,el}}\left(t\right)$ ($\phi_{\mathrm{T},m_{n_0}}^{\mathrm{b,el}}\left(t\right)$), respectively. Correspondingly, $\phi_{\mathrm{R},m_{n_1}}^{\mathrm{f,az}}\left(t\right)$ ($\phi_{\mathrm{R},m_{n_0}}^{\mathrm{b,az}}\left(t\right)$) and $\phi_{\mathrm{R},m_{n_1}}^{\mathrm{f,el}}\left(t\right)$ ($\phi_{\mathrm{R},m_{n_0}}^{\mathrm{b,el}}\left(t\right)$) are AOA and ZOA of the $m$th path of forward (bi-directional) scattering path.

Therefore, the communication CTF between the $p_1$ row and $p_2$ column transmitting antenna and the $u_1$ row and $u_2$ column receiving antenna can be written as

$$\begin{aligned}h_{p_1,p_2,u_1,u_2}^{\mathrm{c}}\left(t,f\right)=&\sqrt{\frac{K_{\mathrm{R}}}{K_{\mathrm{R}}+1}}h_{p_1,p_2,u_1,u_2}^{\mathrm{c,LoS}}\left(t,f\right)\\&+\sqrt{\frac{1}{K_{\mathrm{R}}+1}}\left[h_{p_1,p_2,u_1,u_2}^{\mathrm{c,f}}\left(t,f\right)+h_{p_1,p_2,u_1,u_2}^{\mathrm{c,b}}\left(t,f\right)\right]\end{aligned} \tag{13}$$

where $K_{\mathrm{R}}$ is the Rician factor, $h_{p_1,p_2,u_1,u_2}^{\mathrm{c,LoS}}\left(t,f\right)$, $h_{p_1,p_2,u_1,u_2}^{\mathrm{c,f}}\left(t,f\right)$, and $h_{p_1,p_2,u_1,u_2}^{\mathrm{c,b}}\left(t,f\right)$ are components of LoS, forward scattering, and bi-directional scattering paths, respectively. These three parts of communication CTF can be calculated as

$$h_{p_1,p_2,u_1,u_2}^{\mathrm{c,LoS}}\left(t,f\right)=e^{j\left[2\pi(\omega_{\mathrm{L}}(t)t-f\tau_{\mathrm{c,L}}(t))+\Phi_{\mathrm{L}}\right]}e^{j\frac{2\pi}{\lambda}\Delta d_{\mathrm{L}}^{\mathrm{SW}}(t)} \tag{14}$$

$$h^{\mathrm{c,f}}_{p_1,p_2,u_1,u_2}(t,f) = \sum_{n_1=1}^{N_1(t,f)}\sum_{m=1}^{M_{n_1}} e^{j\left[2\pi\left(\omega_{\mathrm{c},m_{n_1}}(t)t - f\tau_{\mathrm{c},m_{n_1}}(t)\right)+\Phi_{\mathrm{c},m_{n_1}}\right]} \times e^{j\frac{2\pi}{\lambda}\Delta d^{\mathrm{SW}}_{m_{n_1}}(t)} \quad (15)$$

$$h^{\mathrm{c,b}}_{p_1,p_2,u_1,u_2}(t,f) = \sum_{n_0=1}^{N_0(t,f)}\sum_{m=1}^{M_{n_0}} e^{j\left[2\pi\left(\omega_{\mathrm{c},m_{n_0}}(t)t - f\tau_{\mathrm{c},m_{n_0}}(t)\right)+\Phi_{\mathrm{c},m_{n_0}}\right]} \times e^{j\frac{2\pi}{\lambda}\Delta d^{\mathrm{SW}}_{m_{n_0}}(t)}. \quad (16)$$

In the LoS component, $\omega_{\mathrm{L}}(t)$ represents Doppler shift caused by the movement of UE, $\tau_{\mathrm{c,L}}(t)$ means the delay, $\Delta d^{\mathrm{SW}}_{\mathrm{L}}(t)$ means the distance difference caused by antenna spacing. In the NLoS component, Doppler shifts of forward and bi-directional scattering paths are represented as $\omega_{\mathrm{c},m_{n_1}}(t)$ and $\omega_{\mathrm{c},m_{n_0}}(t)$, respectively. Symbol $\tau_{\mathrm{c},m_{n_1}}(t)$ represents the delay of the $m$th path within the $n_1$th cluster of forward scattering part. Similarly, symbol $\tau_{\mathrm{c},m_{n_0}}(t)$ means the delay of the $m$th path in the $n_0$th cluster of bi-directional scattering part. Besides, $\Phi_{\mathrm{L}}$, $\Phi_{\mathrm{c},m_{n_1}}$, and $\Phi_{\mathrm{c},m_{n_0}}$ are random phases of LoS, forward scattering, and bi-directional scattering paths, respectively. Then, $\Delta d^{\mathrm{SW}}_{m_{n_1}}(t)$ ($\Delta d^{\mathrm{SW}}_{m_{n_0}}(t)$) is the distance difference caused by antenna spacing of forward (bi-directional) scattering path, and it can be calculated as

$$\Delta d^{\mathrm{SW}}_{m_{n_{1/0}}}(t) = \Delta d^{\mathrm{SW}}_{\mathrm{T},m_{n_{1/0}}}(t) + \Delta d^{\mathrm{SW}}_{\mathrm{R},m_{n_{1/0}}}(t). \quad (17)$$

where $\Delta d^{\mathrm{SW}}_{\mathrm{T},m_{n_{1/0}}}(t)$ and $\Delta d^{\mathrm{SW}}_{\mathrm{R},m_{n_{1/0}}}(t)$ can be calculated referring to (6)–(7).

For later use, we represent communication CTF in matrix form as

$$\mathbf{H}^{\mathrm{c}}(t,f) = \sqrt{\frac{K_{\mathrm{R}}}{K_{\mathrm{R}}+1}}\mathbf{H}^{\mathrm{c,LoS}}(t,f) + \sqrt{\frac{1}{K_{\mathrm{R}}+1}}\left[\mathbf{H}^{\mathrm{c,f}}(t,f)+\mathbf{H}^{\mathrm{c,b}}(t,f)\right] \quad (18)$$

where

$$\mathbf{H}^{\mathrm{c,LoS}}(t,f) = e^{j[2\pi(\omega_{\mathrm{L}}(t)t - f\tau_{\mathrm{c,L}}(t))+\Phi_{\mathrm{L}}]}\cdot\mathbf{V}_{\mathrm{c,L}}\cdot\left(\mathbf{U}_{\mathrm{c,L}}\right)^{\mathrm{T}} \quad (19)$$

$$\mathbf{H}^{\mathrm{c,f}}(t,f) = \sum_{n_1=1}^{N_1(t,f)}\sum_{m=1}^{M_{n_1}} e^{j\left[2\pi\left(\omega_{\mathrm{c},m_{n_1}}(t)t - f\tau_{\mathrm{c},m_{n_1}}(t)\right)+\Phi_{\mathrm{c},m_{n_1}}\right]} \times \mathbf{V}_{\mathrm{c},m_{n_1}}\cdot\left(\mathbf{U}_{\mathrm{c},m_{n_1}}\right)^{\mathrm{T}} \quad (20)$$

$$\mathbf{H}^{\mathrm{c,b}}(t,f) = \sum_{n_0=1}^{N_0(t,f)}\sum_{m=1}^{M_{n_0}} e^{j\left[2\pi\left(\omega_{\mathrm{c},m_{n_0}}(t)t - f\tau_{\mathrm{c},m_{n_0}}(t)\right)+\Phi_{\mathrm{c},m_{n_0}}\right]} \times \mathbf{V}_{\mathrm{c},m_{n_0}}\cdot\left(\mathbf{U}_{\mathrm{c},m_{n_0}}\right)^{\mathrm{T}}. \quad (21)$$

Array response matrices of transmitting and receiving arrays are calculated as

$$\mathbf{U}_{\mathrm{c,L}} = \mathbf{b}^{\mathrm{BS}}\left(\varphi^{\mathrm{v}}_{\mathrm{T,L}}(t), d_{\mathrm{L}}(t)\right) \otimes \mathbf{a}^{\mathrm{BS}}\left(\varphi^{\mathrm{h}}_{\mathrm{T,L}}(t), d_{\mathrm{L}}(t)\right) \in \mathbf{C}^{P\times 1} \quad (22)$$

$$\mathbf{V}_{\mathrm{c,L}} = \mathbf{b}^{\mathrm{R}}_{\mathrm{c}}\left(\varphi^{\mathrm{v}}_{\mathrm{R,L}}(t), d_{\mathrm{L}}(t)\right) \otimes \mathbf{a}^{\mathrm{R}}_{\mathrm{c}}\left(\varphi^{\mathrm{h}}_{\mathrm{R,L}}(t), d_{\mathrm{L}}(t)\right) \in \mathbf{C}^{Q^{\mathrm{c}}\times 1} \quad (23)$$

$$\mathbf{U}_{\mathrm{c},m_{n_1}/m_{n_0}} = \mathbf{b}^{\mathrm{BS}}\left(\varphi^{\mathrm{v}}_{\mathrm{T},m_{n_1}/m_{n_0}}(t), d^{\mathrm{c},m_{n_{1/0}}}_{\mathrm{T}}(t)\right) \otimes \mathbf{a}^{\mathrm{BS}}\left(\varphi^{\mathrm{h}}_{\mathrm{T},m_{n_1}/m_{n_0}}(t), d^{\mathrm{c},m_{n_{1/0}}}_{\mathrm{T}}(t)\right) \in \mathbf{C}^{P\times 1} \quad (24)$$

$$\mathbf{V}_{\mathrm{c},m_{n_1}/m_{n_0}} = \mathbf{b}^{\mathrm{R}}_{\mathrm{c}}\left(\varphi^{\mathrm{v}}_{\mathrm{R},m_{n_1}/m_{n_0}}(t), d^{\mathrm{c},m_{n_{1/0}}}_{\mathrm{R}}(t)\right) \otimes \mathbf{a}^{\mathrm{R}}_{\mathrm{c}}\left(\varphi^{\mathrm{h}}_{\mathrm{R},m_{n_1}/m_{n_0}}(t), d^{\mathrm{c},m_{n_{1/0}}}_{\mathrm{R}}(t)\right) \in \mathbf{C}^{Q^{\mathrm{c}}\times 1}. \quad (25)$$

Here, $\varphi^{\mathrm{h}}_{\mathrm{T(R),L}}(t) = -\sin\left(\phi^{\mathrm{L,az}}_{\mathrm{T(R)}}(t)\right)\cos\left(\phi^{\mathrm{L,el}}_{\mathrm{T(R)}}(t)\right)$, $\varphi^{\mathrm{v}}_{\mathrm{T(R),L}}(t) = -\sin\left(\phi^{\mathrm{L,el}}_{\mathrm{T(R)}}(t)\right)$, $\varphi^{\mathrm{h}}_{\mathrm{T(R)},m_{n_1}/m_{n_0}}(t) = -\sin\left(\phi^{\mathrm{f/b,az}}_{\mathrm{T(R)},m_{n_1}/m_{n_0}}(t)\right)\cos\left(\phi^{\mathrm{f/b,el}}_{\mathrm{T(R)},m_{n_1}/m_{n_0}}(t)\right)$, and $\varphi^{\mathrm{v}}_{\mathrm{T(R)},m_{n_1}/m_{n_0}}(t) = -\sin\left(\phi^{\mathrm{f/b,el}}_{\mathrm{T(R)},m_{n_1}/m_{n_0}}(t)\right)$ are the spatial frequencies in azimuth and elevation directions for the LoS and forward/bi-directional scattering paths at the Tx (Rx) side. The calculation of $\mathbf{U}_{\mathrm{c,L}}$ and $\mathbf{U}_{\mathrm{c},m_{n_1}/m_{n_0}}$ can refer to (9)–(10). Furthermore, vectors $\mathbf{a}^{\mathrm{R}}_{\mathrm{c}}(\varphi(t), d(t))$ and $\mathbf{b}^{\mathrm{R}}_{\mathrm{c}}(\varphi(t), d(t))$ can be calculated by substituting $u_1$ and $u_2$ for $q_1$ and $q_2$ in (11) and (12), respectively. The generation method of the delay, distance, AOD, ZOD, AOA, and ZOA parameters and random phases is detailed in [41]. The difference is that the sensing and communication GBSMs here has the space-time-frequency non-stationarity. Given that the VR method can only describe spatial non-stationarity, the birth-death process of clusters is adopted to uniformly model the spatial-time-frequency non-stationarity.

### C. Birth-death Process

Both the set of sensing channel clusters $S_{p_1,p_2,q_1,q_2}(t,f)$ and the set of communication channel clusters $C_{p_1,p_2,u_1,u_2}(t,f)$ need to be generated using the birth-death process. Considering the similarity in the birth-death processes of clusters in sensing and communication channels, we take the generation process of $S_{p_1,p_2,q_1,q_2}(t,f)$ of the sensing channel as an example. The changes of set $S_{p_1,p_2,q_1,q_2}(t,f)$ along the array-time-frequency axes can be represented as the sum of remaining clusters and new clusters, i.e., $S_{p_1,p_2,q_1,q_2}(t,f) = S^{re}_{p_1,p_2,q_1,q_2}(t,f) + S^{new}_{p_1,p_2,q_1,q_2}(t,f)$. The intervals between transmitting and receiving antennas are $\Delta_{\mathrm{T},p_1p_2p_1{}'p_2{}'}$ and $\Delta_{\mathrm{R},q_1q_2q_1{}'q_2{}'}$, respectively. The time interval is $\Delta t$, and the frequency interval is $\Delta f$. The cluster survival probability is the product of the survival probabilities on the array axis, time axis, and frequency axis, i.e.,

$$P_{\mathrm{re}}\left(\Delta_{\mathrm{T},p_1p_2p_1'p_2'}, \Delta_{\mathrm{R},q_1q_2q_1'q_2'}, \Delta t, \Delta f\right) = P_{\mathrm{re}}\left(\Delta_{\mathrm{T},p_1p_2p_1'p_2'}\right)P_{\mathrm{re}}\left(\Delta_{\mathrm{R},q_1q_2q_1'q_2'}\right)P_{\mathrm{re}}(\Delta t)\,P_{\mathrm{re}}(\Delta f). \quad (26)$$

The remaining probabilities of the cluster on the axis of transmitting and receiving antenna arrays are $P_{\mathrm{re}}\left(\Delta_{\mathrm{T},p_1p_2p_1'p_2'}\right) = \mathrm{e}^{-\lambda_{\mathrm{D}}\frac{\Delta_{\mathrm{T},p_1p_2p_1'p_2'}}{D^{\mathrm{A}}_{\mathrm{c}}}}$ and $P_{\mathrm{re}}\left(\Delta_{\mathrm{R},q_1q_2q_1'q_2'}\right) = \mathrm{e}^{-\lambda_{\mathrm{D}}\frac{\Delta_{\mathrm{R},q_1q_2q_1'q_2'}}{D^{\mathrm{A}}_{\mathrm{c}}}}$, respectively. Besides, $P_{\mathrm{re}}(\Delta t) = \mathrm{e}^{-\lambda_{\mathrm{D}}\frac{v_{s,k_l}\cdot\Delta t}{D^{\mathrm{T}}_{\mathrm{c}}}}$ and $P_{\mathrm{re}}(\Delta f) = \mathrm{e}^{-\lambda_{\mathrm{D}}\frac{F(\Delta f)}{D^{\mathrm{F}}_{\mathrm{c}}}}$ are remaining probabilities of the cluster on the time axis and the frequency axis, respectively. Here, $D^{\mathrm{A/T/F}}_{\mathrm{c}}$ is the

$$\Psi_{\mathrm{T}}^{\mathrm{h}}\left(\alpha\left(t\right),d\left(t\right)\right)=e^{j\frac{2\pi}{\lambda}\left\{(p_1-1)\Delta_{\mathrm{T}}\left[\alpha(t)-\tilde{\varphi}_{\mathrm{T},p_1}^{\mathrm{h}}\right]+\frac{(p_1-1)^2\Delta_{\mathrm{T}}{}^2\left[\left(\tilde{\varphi}_{\mathrm{T},p_1}^{\mathrm{h}}\right)^2-\alpha^2(t)\right]}{2d(t)}\right\}} \tag{29}$$

$$\Psi_{\mathrm{T}}^{\mathrm{v}}\left(\alpha\left(t\right),d\left(t\right)\right)=e^{j\frac{2\pi}{\lambda}\left\{(p_2-1)\Delta_{\mathrm{T}}\left[\alpha(t)-\tilde{\varphi}_{\mathrm{T},p_2}^{\mathrm{v}}\right]+\frac{(p_2-1)^2\Delta_{\mathrm{T}}{}^2\left[\left(\tilde{\varphi}_{\mathrm{T},p_2}^{\mathrm{v}}\right)^2-\alpha^2(t)\right]}{2d(t)}\right\}} \tag{30}$$

$$\Psi_{\mathrm{Rs}}^{\mathrm{h}}\left(\alpha\left(t\right),d\left(t\right)\right)=e^{j\frac{2\pi}{\lambda}\left\{(q_1-1)\Delta_{\mathrm{R}}\left[\alpha(t)-\tilde{\varphi}_{\mathrm{R},q_1}^{\mathrm{h}}\right]+\frac{(q_1-1)^2\Delta_{\mathrm{R}}{}^2\left[\left(\tilde{\varphi}_{\mathrm{R},q_1}^{\mathrm{h}}\right)^2-\alpha^2(t)\right]}{2d(t)}\right\}} \tag{31}$$

$$\Psi_{\mathrm{Rs}}^{\mathrm{v}}\left(\alpha\left(t\right),d\left(t\right)\right)=e^{j\frac{2\pi}{\lambda}\left\{(q_2-1)\Delta_{\mathrm{R}}\left[\alpha(t)-\tilde{\varphi}_{\mathrm{R},q_2}^{\mathrm{v}}\right]+\frac{(q_2-1)^2\Delta_{\mathrm{R}}{}^2\left[\left(\tilde{\varphi}_{\mathrm{R},q_2}^{\mathrm{v}}\right)^2-\alpha^2(t)\right]}{2d(t)}\right\}}. \tag{32}$$

correlation factor on the space/time/frequency axis, which should be determined by the scenario [48]. Symbol $F\left(\Delta f\right)$ is a parameter that can be determined by measurement results [49], $\lambda_{\mathrm{D}}$ represents the death probability of the cluster. After experiencing a transmitting/receiving antenna interval $\Delta_{\mathrm{T},p_1p_2p_1{}'p_2{}'}/\Delta_{\mathrm{R},q_1q_2q_1{}'q_2{}'}$, time interval $\Delta t$, and frequency interval $\Delta f$, the number of newly generated clusters is calculated as $E\left[\mathrm{L_{new}}\right]=\frac{\lambda_{\mathrm{G}}}{\lambda_{\mathrm{D}}}\left[1-P_{\mathrm{re}}\left(\Delta_{\mathrm{T},p_1p_2p_1{}'p_2{}'},\Delta_{\mathrm{R},q_1q_2q_1{}'q_2{}'},\Delta t,\Delta f\right)\right]$, where $\lambda_{\mathrm{G}}$ is the birth rate of clusters.

## III. A Novel 3D Non-stationary mmWave Massive MIMO ISAC BDCM

The GBSM describes the multipath between transmitting and receiving antennas, superposing the multipath between transmitting and receiving antennas to obtain the channel matrix. Unlike GBSM, the BDCM equally divides antenna domain into multiple beam domain, and describes the attenuation of the channel between each pair of transmitting and receiving beams [50], [51]. By performing beamforming, paths from different antennas are coherently stacked to form a channel matrix in the beam domain [52]. This is important for massive MIMO, where the number of antennas is so large that BDCM can effectively reflect the sparse characteristics of the channel, thereby reducing the complexity of channel modeling [53]. In addition, for the sensing channel, BDCM can effectively reflect in which beam direction obstacles are located, which is helpful for long-range target recognition and tracking. BDCM also plays a guiding role in the beamforming and beam prediction of the ISAC system. Therefore, it is necessary to study BDCM and explore its channel characteristics.

### A. Sensing Channel Modeling

The sensing BDCM can be obtained by performing beamforming operations on CTF matrix of sensing GBSM,

$$\mathbf{H}_{\mathrm{B}}^{\mathrm{s}}\left(t,f\right)=\tilde{\mathbf{V}}_{\mathrm{s}}^{\mathrm{H}}\mathbf{H}^{\mathrm{s}}\left(t,f\right)\tilde{\mathbf{U}} \tag{27}$$

where $\left(\cdot\right)^{\mathrm{H}}$ means conjugate transpose operation, $\tilde{\mathbf{U}}=\frac{1}{\sqrt{P}}\tilde{\mathbf{U}}_{\mathrm{el}}\otimes\tilde{\mathbf{U}}_{\mathrm{az}}$ and $\tilde{\mathbf{V}}_{\mathrm{s}}=\frac{1}{\sqrt{Q^{\mathrm{s}}}}\tilde{\mathbf{V}}_{\mathrm{s,el}}\otimes\tilde{\mathbf{V}}_{\mathrm{s,az}}$ are beamforming matrices at Tx and sensing Rx, respectively. The uniform spatial frequency response matrices in azimuth and elevation directions for Tx and sensing Rx are denoted as $\tilde{\mathbf{U}}_{\mathrm{az}}=\left[\mathbf{a}^{\mathrm{BS}}\left(\tilde{\varphi}_{\mathrm{T},p_1}^{\mathrm{h}},d\left(t\right)\right)\right]_{p_1=1,\ldots,P_{\mathrm{h}}}$, $\tilde{\mathbf{U}}_{\mathrm{el}}=\left[\mathbf{b}^{\mathrm{BS}}\left(\tilde{\varphi}_{\mathrm{T},p_2}^{\mathrm{v}},d\left(t\right)\right)\right]_{p_2=1,\ldots,P_{\mathrm{v}}}$, $\tilde{\mathbf{V}}_{\mathrm{s,az}}=\left[\mathbf{a}_{\mathrm{s}}^{\mathrm{R}}\left(\tilde{\varphi}_{\mathrm{R},q_1}^{\mathrm{h}},d\left(t\right)\right)\right]_{q_1=1,\ldots,Q_{\mathrm{h}}^{\mathrm{s}}}$, and $\tilde{\mathbf{V}}_{\mathrm{s,el}}=\left[\mathbf{b}_{\mathrm{s}}^{\mathrm{R}}\left(\tilde{\varphi}_{\mathrm{R},q_2}^{\mathrm{v}},d\left(t\right)\right)\right]_{q_2=1,\ldots,Q_{\mathrm{v}}^{\mathrm{s}}}$. The spatial frequencies can be represented as $\tilde{\varphi}_{\mathrm{T},p_1}^{\mathrm{h}}=\frac{2p_1-1}{P_{\mathrm{h}}}-1$, $\tilde{\varphi}_{\mathrm{T},p_2}^{\mathrm{v}}=\frac{2p_2-1}{P_{\mathrm{v}}}-1$, $\tilde{\varphi}_{\mathrm{R},q_1}^{\mathrm{h}}=\frac{2q_1-1}{Q_{\mathrm{h}}^{\mathrm{s}}}-1$, and $\tilde{\varphi}_{\mathrm{R},q_2}^{\mathrm{v}}=\frac{2q_2-1}{Q_{\mathrm{v}}^{\mathrm{s}}}-1$, which divide the spaces on both Tx and sensing Rx sides into equal parts $P_{\mathrm{h(v)}}^{\mathrm{s}}$ and $Q_{\mathrm{h(v)}}^{\mathrm{s}}$ in the horizontal (vertical) directions, respectively. The element $h_{\mathrm{B},p_1,p_2,q_1,q_2}^{\mathrm{s}}\left(t,f\right)$ in $\mathbf{H}_{\mathrm{B}}^{\mathrm{s}}\left(t,f\right)$ means the sensing CTF between the $p_1$th horizontal $p_2$th vertical transmitting beam and the $q_1$th horizontal $q_2$th vertical receiving beam. Therefore, $h_{\mathrm{B},p_1,p_2,q_1,q_2}^{\mathrm{s}}\left(t,f\right)$ can be further expressed as

$$\begin{aligned}
&h_{\mathrm{B},p_1,p_2,q_1,q_2}^{\mathrm{s}}\left(t,f\right)\\
&=\sum_{l=1}^{\mathrm{L}(t,f)}\sum_{k=1}^{K_l}\frac{1}{\sqrt{PQ^{\mathrm{s}}}}\beta_{\mathrm{s},k_l}e^{j\left[2\pi\left(\omega_{\mathrm{s},k_l}(t)t-f\tau_{\mathrm{s},k_l}(t)\right)+\Phi_{\mathrm{s},k_l}\right]}\\
&\times\sum_{q_2=1}^{Q_{\mathrm{v}}^{\mathrm{s}}}\Psi_{\mathrm{Rs}}^{\mathrm{v}}\left(\varphi_{\mathrm{R},k_l}^{\mathrm{v}}\left(t\right),d_{\mathrm{R}}^{\mathrm{s},k_l}\left(t\right)\right)\sum_{q_1=1}^{Q_{\mathrm{h}}^{\mathrm{s}}}\Psi_{\mathrm{Rs}}^{\mathrm{h}}\left(\varphi_{\mathrm{R},k_l}^{\mathrm{h}}\left(t\right),d_{\mathrm{R}}^{\mathrm{s},k_l}\left(t\right)\right)\\
&\times\sum_{p_2=1}^{P_{\mathrm{v}}}\Psi_{\mathrm{T}}^{\mathrm{v}}\left(\varphi_{\mathrm{T},k_l}^{\mathrm{v}}\left(t\right),d_{\mathrm{T}}^{\mathrm{s},k_l}\left(t\right)\right)\sum_{p_1=1}^{P_{\mathrm{h}}}\Psi_{\mathrm{T}}^{\mathrm{h}}\left(\varphi_{\mathrm{T},k_l}^{\mathrm{h}}\left(t\right),d_{\mathrm{T}}^{\mathrm{s},k_l}\left(t\right)\right).
\end{aligned} \tag{28}$$

where $\Psi_{\mathrm{T}}^{\mathrm{h}}\left(\alpha\left(t\right),d\left(t\right)\right)$, $\Psi_{\mathrm{T}}^{\mathrm{v}}\left(\alpha\left(t\right),d\left(t\right)\right)$, $\Psi_{\mathrm{Rs}}^{\mathrm{h}}\left(\alpha\left(t\right),d\left(t\right)\right)$, and $\Psi_{\mathrm{Rs}}^{\mathrm{v}}\left(\alpha\left(t\right),d\left(t\right)\right)$ can be calculated by (29)–(32) written at the top of this page.

### B. Communication Channel Modeling

By performing beamforming operations on communication GBSM $\mathbf{H}^{\mathrm{c}}\left(t,f\right)$ to obtain the communication BDCM, the communication BDCM can also be expressed as LoS $\mathbf{H}_{\mathrm{B}}^{\mathrm{c,LoS}}\left(t,f\right)$, forward scattering $\mathbf{H}_{\mathrm{B}}^{\mathrm{c,f}}\left(t,f\right)$, and bi-directional scattering $\mathbf{H}_{\mathrm{B}}^{\mathrm{c,b}}\left(t,f\right)$ three components. The communication BDCM can be calculated as

$$\begin{aligned}
\mathbf{H}_{\mathrm{B}}^{\mathrm{c}}\left(t,f\right)&=\tilde{\mathbf{V}}_{\mathrm{c}}^{H}\mathbf{H}^{\mathrm{c}}\left(t,f\right)\tilde{\mathbf{U}}\\
&=\sqrt{\frac{K_{\mathrm{R}}}{K_{\mathrm{R}}+1}}\mathbf{H}_{\mathrm{B}}^{\mathrm{c,LoS}}\left(t,f\right)\\
&\quad+\sqrt{\frac{1}{K_{\mathrm{R}}+1}}\left[\mathbf{H}_{\mathrm{B}}^{\mathrm{c,f}}\left(t,f\right)+\mathbf{H}_{\mathrm{B}}^{\mathrm{c,b}}\left(t,f\right)\right]
\end{aligned} \tag{33}$$

where $\tilde{\mathbf{U}}$ is defined the same as that in (27). Besides, $\tilde{\mathbf{V}}_{\mathrm{c}}=\frac{1}{\sqrt{Q^{\mathrm{c}}}}\tilde{\mathbf{V}}_{\mathrm{c,el}}\otimes\tilde{\mathbf{V}}_{\mathrm{c,az}}$ represents the beamforming matrix

of UE, in which $\tilde{\mathbf{V}}_{\mathrm{c,az}} = \left[\mathbf{a}_{\mathrm{c}}^{\mathrm{R}}\left(\tilde{\varphi}_{\mathrm{R},u_1}^{\mathrm{h}}, d\left(t\right)\right)\right]_{u_1=1,\ldots,Q_{\mathrm{h}}^{\mathrm{c}}}$ and $\tilde{\mathbf{V}}_{\mathrm{c,el}} = \left[\mathbf{b}_{\mathrm{c}}^{\mathrm{R}}\left(\tilde{\varphi}_{\mathrm{R},u_2}^{\mathrm{v}}, d\left(t\right)\right)\right]_{u_2=1,\ldots,Q_{\mathrm{v}}^{\mathrm{c}}}$. The spatial frequencies in the horizontal and vertical directions are $\tilde{\varphi}_{\mathrm{R},u_1}^{\mathrm{h}} = \frac{2u_1-1}{Q_{\mathrm{h}}^{\mathrm{c}}} - 1$ and $\tilde{\varphi}_{\mathrm{R},u_2}^{\mathrm{v}} = \frac{2u_2-1}{Q_{\mathrm{v}}^{\mathrm{c}}} - 1$, respectively. Then, the elements of communication BDCM matrix can be written as

$$\begin{aligned} &h_{\mathrm{B},p_1,p_2,u_1,u_2}^{\mathrm{c,LoS}}\left(t,f\right) = e^{j\left[2\pi\left(\omega_{\mathrm{L}}\left(t\right)t - f\tau_{\mathrm{c,L}}\left(t\right)\right)+\Phi_{\mathrm{L}}\right]} \\ &\times \sum_{u_2=1}^{Q_{\mathrm{v}}^{\mathrm{c}}} \Psi_{\mathrm{Rc}}^{\mathrm{v}}\left(\varphi_{\mathrm{R,L}}^{\mathrm{v}}\left(t\right), d_{\mathrm{L}}\left(t\right)\right) \times \sum_{u_1=1}^{Q_{\mathrm{h}}^{\mathrm{c}}} \Psi_{\mathrm{Rc}}^{\mathrm{h}}\left(\varphi_{\mathrm{R,L}}^{\mathrm{h}}\left(t\right), d_{\mathrm{L}}\left(t\right)\right) \\ &\times \sum_{p_2=1}^{P_{\mathrm{v}}} \Psi_{\mathrm{T}}^{\mathrm{v}}\left(\varphi_{\mathrm{T,L}}^{\mathrm{v}}\left(t\right), d_{\mathrm{L}}\left(t\right)\right) \times \sum_{p_1=1}^{P_{\mathrm{h}}} \Psi_{\mathrm{T}}^{\mathrm{h}}\left(\varphi_{\mathrm{T,L}}^{\mathrm{h}}\left(t\right), d_{\mathrm{L}}\left(t\right)\right) \end{aligned} \tag{34}$$

$$\begin{aligned} &h_{\mathrm{B},p_1,p_2,u_1,u_2}^{\mathrm{c,f}}\left(t,f\right) \\ &= \sum_{n_1=1}^{N_1(t,f)} \sum_{m=1}^{M_{n_1}} e^{j\left[2\pi\left(\omega_{\mathrm{c},m_{n_1}}\left(t\right)t - f\tau_{\mathrm{c},m_{n_1}}\left(t\right)\right)+\Phi_{\mathrm{c},m_{n_1}}\right]} \\ &\times \sum_{u_2=1}^{Q_{\mathrm{v}}^{\mathrm{c}}} \Psi_{\mathrm{Rc}}^{\mathrm{v}}\left(\varphi_{\mathrm{R},m_{n_1}}^{\mathrm{v}}\left(t\right), d_{\mathrm{R}}^{\mathrm{c},m_{n_1}}\left(t\right)\right) \\ &\times \sum_{u_1=1}^{Q_{\mathrm{h}}^{\mathrm{c}}} \Psi_{\mathrm{Rc}}^{\mathrm{h}}\left(\varphi_{\mathrm{R},m_{n_1}}^{\mathrm{h}}\left(t\right), d_{\mathrm{R}}^{\mathrm{c},m_{n_1}}\left(t\right)\right) \\ &\times \sum_{p_2=1}^{P_{\mathrm{v}}} \Psi_{\mathrm{T}}^{\mathrm{v}}\left(\varphi_{\mathrm{T},m_{n_1}}^{\mathrm{v}}\left(t\right), d_{\mathrm{T}}^{\mathrm{c},m_{n_1}}\left(t\right)\right) \\ &\times \sum_{p_1=1}^{P_{\mathrm{h}}} \Psi_{\mathrm{T}}^{\mathrm{h}}\left(\varphi_{\mathrm{T},m_{n_1}}^{\mathrm{h}}\left(t\right), d_{\mathrm{T}}^{\mathrm{c},m_{n_1}}\left(t\right)\right) \end{aligned} \tag{35}$$

Furthermore, $h_{\mathrm{B},p_1,p_2,u_1,u_2}^{\mathrm{c,b}}\left(t,f\right)$ can be obtained by replacing the forward scattering parameters in (35) with the bi-directional scattering parameters. Here, $\Psi_{\mathrm{Rc}}^{\mathrm{h}}\left(\alpha\left(t\right), d\left(t\right)\right)$ can be claculated substituting $q_1$ and $\tilde{\varphi}_{\mathrm{R},q_1}^{\mathrm{h}}$ by $u_1$ and $\tilde{\varphi}_{\mathrm{R},u_1}^{\mathrm{h}}$ in (31), respectively. Similarly, $\Psi_{\mathrm{Rc}}^{\mathrm{v}}\left(\alpha\left(t\right), d\left(t\right)\right)$ can be obtained substituting $q_2$ and $\tilde{\varphi}_{\mathrm{R},q_2}^{\mathrm{v}}$ by $u_2$ and $\tilde{\varphi}_{\mathrm{R},u_2}^{\mathrm{v}}$ in (32), respectively.

The amplitudes of $\mathbf{H}_{\mathrm{B}}^{\mathrm{s}}\left(t,f\right)$ and $\mathbf{H}_{\mathrm{B}}^{\mathrm{c}}\left(t,f\right)$ represent the degrees of coupling between transmitting and receiving beams of sensing and communication BDCMs, respectively. When the transmitting array is a $32 \times 32$ UPA, the contours of sensing BDCM and communication BDCM are shown in Figs. 2 (a) and (b), respectively. It can be seen that the communication BDCM exhibits more significant sparsity than the sensing BDCM. The reason is that the transmitting and receiving arrays of the mono-static sensing channel are located at the same location, and the sensing channel is composed of sensing echoes caused by single-bounce backward scattering clusters. Therefore, there is a higher degree of beam coupling between the sensing transmitting and receiving sides than that of the communication channel. Moreover, there exist areas where both the sensing and communication channels have relatively large amplitudes (circled with red dotted lines in Fig. 2), which demonstrates the existence of the shared first-bounce cluster caused by backscattering in sensing and communication channels.

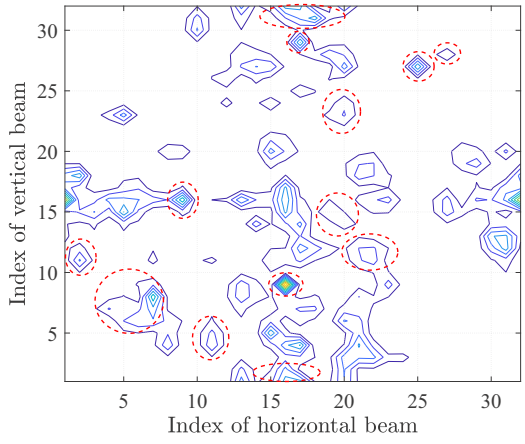


(a) Sensing BDCM $\mathbf{H}_{\mathrm{B}}^{\mathrm{s}}\left(t,f\right)$

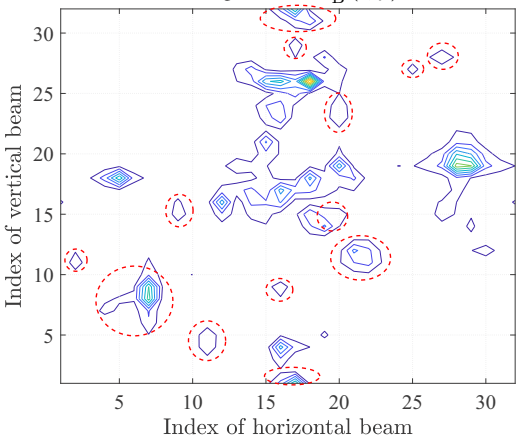


(b) Communication BDCM $\mathbf{H}_{\mathrm{B}}^{\mathrm{c}}\left(t,f\right)$

Fig. 2. Contours of (a) sensing BDCM $\mathbf{H}_{\mathrm{B}}^{\mathrm{s}}\left(t,f\right)$ and (b) communication BDCM $\mathbf{H}_{\mathrm{B}}^{\mathrm{c}}\left(t,f\right)$ ($f_c$ = 28 GHz, $P_h = P_v = Q_{\mathrm{h}}^{\mathrm{s}} = Q_{\mathrm{v}}^{\mathrm{s}} = Q_{\mathrm{h}}^{\mathrm{c}} = Q_{\mathrm{v}}^{\mathrm{c}}$ = 32, $d_{\mathrm{L}}$ = 100 m, $v_{\mathrm{R}}\left(t\right)$ = 0 m/s, $L$ = 10, $K_l$ = 10, $N_1 = N_0$ = 5, $M_{n_1} = M_{n_0}$ = 10, $v_{\mathrm{s},k_l}\left(t\right) = v_{m_{n_1}}^{\mathrm{f}}\left(t\right) = v_{m_{n_0}}^{\mathrm{b}}\left(t\right)$ = 0 m/s).

Figs. 3 (a) and (b) compare the beamwidths calculated by the proposed general steering vector and the traditional planar wavefront steering vector when carrier frequencies are $f_c$ = 2.6 GHz and 28 GHz, respectively. We set the distance from the BS to the first-bounce cluster as 5 m. It can be observed in Fig. 3 (a) that when $f_c$ = 2.6 GHz, the beamwidth generated by the general steering vector is narrower than that generated by the traditional steering vector. This indicates that traditional steering vectors underestimate the ability of large-scale antenna arrays to narrow the beamwidth under the near-field spherical wavefront assumption. In addition, when $f_c$ = 28 GHz, the beamwidth simulation results generated by two steering vectors are compared in Fig. 3 (b). There is no significant difference between these two beamwidth simulation results. This is because the antenna spacing is determined by the wavelength, and the array aperture decreases correspondingly as the carrier frequency increases. The reduction of antenna array aperture results in the reduction of Rayleigh distance, which leads to the spherical wavefront approximating the planar wavefront. Therefore, the proposed steering vector can be simplified to traditional steering vectors. Moreover, the simulation results illustrate that the proposed steering vector exhibits good generality, both in the case of far-field planar

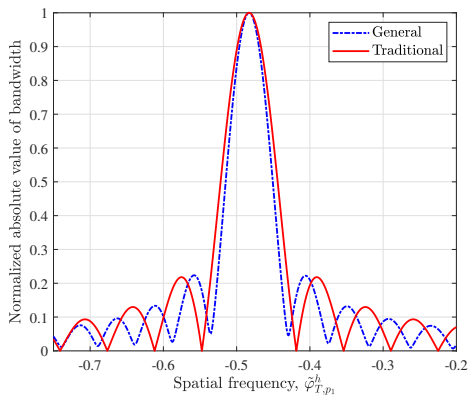


(a)

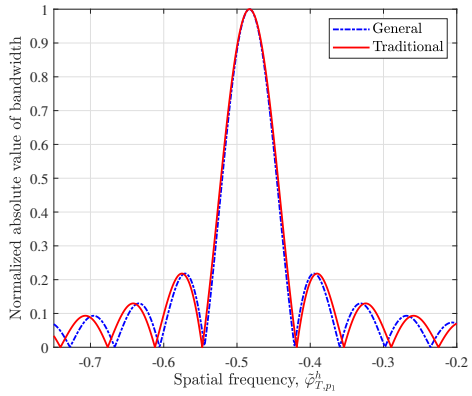


(b)

Fig. 3. Beamwidths of the general steering vector and the planar wavefront steering vector when (a) $f_c$ = 2.6 GHz, spherical wavefront and (b) $f_c$ = 28 GHz, plane wavefront.

wavefront and near-field spherical wavefront assumptions.

## IV. Statistical Properties of the GBSM and BDCM

Statistical properties illustrate channel characteristics more intuitively [54]. To compare and analyze the differences and correlations between the sensing and communication channels, some typical statistical properties are studied, including STF-CF, RMS beam spread, RMS delay spread, temporary Doppler PSD, and coherence time. In addition, as an important indicator of the communication system, the channel capacity is also studied in this section.

### A. STF-CF

The STF-CFs of GBSM (BDCM) are derived here. The STF-CF between the sensing GBSM (BDCM) $h^{\mathrm{s}}_{(\mathrm{B}),p_1,p_2,q_1,q_2}(t,f)$ and $h^{\mathrm{s}}_{(\mathrm{B}),p_1',p_2',q_1',q_2'}(t+\Delta t,f+\Delta f)$ can be calculated as

$$\begin{aligned}&R^{\mathrm{s}}_{(\mathrm{B}),p_1p_2q_1q_2p_1'p_2'q_1'q_2'}(t,f,\Delta t,\Delta f)\\&=E\left\{h^{\mathrm{s}}_{(\mathrm{B}),p_1,p_2,q_1,q_2}(t,f)\cdot h^{\mathrm{s}*}_{(\mathrm{B}),p_1',p_2',q_1',q_2'}(t+\Delta t,f+\Delta f)\right\}\end{aligned} \tag{36}$$

where $E\{\cdot\}$ denotes expectation, $(\cdot)^*$ represents the complex conjugation.

In the same way, the STF-CF between $h^{\mathrm{c}}_{(\mathrm{B}),p_1,p_2,u_1,u_2}(t,f)$ and $h^{\mathrm{c}}_{(\mathrm{B}),p_1',p_2',u_1',u_2'}(t+\Delta t,f+\Delta f)$ of communication GBSM can be written as

$$\begin{aligned}&R^{\mathrm{c}}_{(\mathrm{B}),p_1p_2u_1u_2p_1'p_2'u_1'u_2'}(t,f,\Delta t,\Delta f)\\&=E\left\{h^{\mathrm{c}}_{(\mathrm{B}),p_1,p_2,u_1,u_2}(t,f)\cdot h^{\mathrm{c}*}_{(\mathrm{B}),p_1',p_2',u_1',u_2'}(t+\Delta t,f+\Delta f)\right\}\\&=\frac{K_{\mathrm{R}}}{K_{\mathrm{R}}+1}\cdot R^{\mathrm{c,LoS}}_{(\mathrm{B}),p_1p_2u_1u_2p_1'p_2'u_1'u_2'}(t,f,\Delta t,\Delta f)\\&+P_{\mathrm{re}}\left(\Delta_{\mathrm{T},p_1p_2p_1'p_2'},\Delta_{\mathrm{R},u_1u_2u_1'u_2'},\Delta t,\Delta f\right)\cdot\frac{1}{K_{\mathrm{R}}+1}\\&\times\left[R^{\mathrm{c,f}}_{(\mathrm{B}),p_1p_2u_1u_2p_1'p_2'u_1'u_2'}(t,f,\Delta t,\Delta f)\right.\\&\left.+R^{\mathrm{c,b}}_{(\mathrm{B}),p_1p_2u_1u_2p_1'p_2'u_1'u_2'}(t,f,\Delta t,\Delta f)\right]\end{aligned} \tag{37}$$

where $R^{\mathrm{c,LoS/f/b}}_{(\mathrm{B}),p_1p_2u_1u_2p_1'p_2'u_1'u_2'}(t,f,\Delta t,\Delta f)$ is STF-CF of communication LoS/forward scattering/bi-directional scattering component. These three components can be calculated as

$$\begin{aligned}&R^{\mathrm{c,LoS/f/b}}_{(\mathrm{B}),p_1p_2u_1u_2p_1'p_2'u_1'u_2'}(t,f,\Delta t,\Delta f)\\&=E\left\{h^{\mathrm{c,LoS/f/b}}_{(\mathrm{B}),p_1,p_2,u_1,u_2}(t,f)\cdot h^{\mathrm{c,LoS/f/b}*}_{(\mathrm{B}),p_1',p_2',u_1',u_2'}(t+\Delta t,f+\Delta f)\right\}\end{aligned} \tag{38}$$

where the subscript B means the CFs of BDCMs. By setting $\Delta t=0$ and $\Delta f=0$, the STF-CFs can be simplified to spatial cross-correlation functions (SCCFs). In addition, by setting $\Delta_{\mathrm{T},p_1p_2p_1'p_2'}=0$, $\Delta_{\mathrm{R},q_1q_2q_1'q_2'}=0$, $\Delta_{\mathrm{R},u_1u_2u_1'u_2'}=0$, and $\Delta f=0$, the temporal autocorrelation functions (TACFs) can be obtained. Furthermore, the frequency correlation functions (FCFs) can be obtained by setting $\Delta_{\mathrm{T},p_1p_2p_1'p_2'}=0$, $\Delta_{\mathrm{R},,q_1q_2q_1'q_2'}=0$, $\Delta_{\mathrm{R},u_1u_2u_1'u_2'}=0$, and $\Delta t=0$.

### B. RMS Beam and Delay Spreads

The beam spread gives an expression of the dispersion of channel power in different beam directions. The RMS beam spread in azimuth at the Tx side of the sensing BDCM is denoted as

$$\begin{aligned}&\sigma^{\mathrm{s,az}}_{\mathrm{T},B}\\&=\sqrt{\frac{\sum_{p_1,p_2,q_1,q_2=1}^{P_{\mathrm{h}},P_{\mathrm{v}},Q^{\mathrm{s}}_{\mathrm{h}},Q^{\mathrm{s}}_{\mathrm{v}}}\left|h^{\mathrm{s}}_{\mathrm{B},p_1,p_2,q_1,q_2}(t,f)\right|^2\left(\tilde{\varphi}^{\mathrm{h}}_{\mathrm{T},p_1}-\mu^{\mathrm{s,az}}_{\mathrm{T}}\right)^2}{\sum_{p_1,p_2,q_1,q_2=1}^{P_{\mathrm{h}},P_{\mathrm{v}},Q^{\mathrm{s}}_{\mathrm{h}},Q^{\mathrm{s}}_{\mathrm{v}}}\left|h^{\mathrm{s}}_{\mathrm{B},p_1,p_2,q_1,q_2}(t,f)\right|^2}}\end{aligned} \tag{39}$$

where $\mu^{\mathrm{s,az}}_{\mathrm{T}}$ is the power weighted average of transmitting azimuth beams,

$$\mu^{\mathrm{s,az}}_{\mathrm{T}}=\frac{\sum_{p_1,p_2,q_1,q_2=1}^{P_{\mathrm{h}},P_{\mathrm{v}},Q^{\mathrm{s}}_{\mathrm{h}},Q^{\mathrm{s}}_{\mathrm{v}}}\left|h^{\mathrm{s}}_{\mathrm{B},p_1,p_2,q_1,q_2}(t,f)\right|^2\cdot\tilde{\varphi}^{\mathrm{h}}_{\mathrm{T},p_1}}{\sum_{p_1,p_2,q_1,q_2=1}^{P_{\mathrm{h}},P_{\mathrm{v}},Q^{\mathrm{s}}_{\mathrm{h}},Q^{\mathrm{s}}_{\mathrm{v}}}\left|h^{\mathrm{s}}_{\mathrm{B},p_1,p_2,q_1,q_2}(t,f)\right|^2}. \tag{40}$$

The delay spread demonstrates the multipath transmission effect, which refers to the difference in arrival times of multipaths at the Rx. In addition, the delay spread also indicates the power distribution over the delay domain. In order to obtain the RMS delay spread $\sigma^{\mathrm{s}}_{\mathrm{B},DS}$ of the sensing channel, we can substitute $\tilde{\varphi}^{\mathrm{h}}_{\mathrm{T},p_1}$ and $\mu^{\mathrm{s,az}}_{\mathrm{T}}$ to $\tau_{\mathrm{s},k_l}$ and $\mu^{\mathrm{s}}_{DS}$ in (39) and (40), respectively. Here, $\mu^{\mathrm{s}}_{DS}$ denotes the mean value of the power weighted delay. The calculation of the RMS beam spread and RMS delay spread for the communication BDCM is similar to that for the sensing BDCM. The difference is that the LoS, forward scattering, and bi-directional scattering components

need to be considered when calculating the RMS beam spread of the communication BDCM, i.e.,

$$\sigma_{\mathrm{T,B}}^{\mathrm{c,az}}=\sigma_{\mathrm{T,B}}^{\mathrm{c},az,\mathrm{L}}+\sigma_{\mathrm{T,B}}^{\mathrm{c},az,f}+\sigma_{\mathrm{T,B}}^{\mathrm{c},az,b} \tag{41}$$

where

$$\sigma_{\mathrm{T,B}}^{\mathrm{c,az,L/f/b}}= \sqrt{\frac{\sum_{p_1,p_2,u_1,u_2=1}^{P_{\mathrm{h}},P_{\mathrm{v}},Q_{\mathrm{h}}^{\mathrm{c}},Q_{\mathrm{v}}^{\mathrm{c}}}\left|h_{\mathrm{B},p_1,p_2,u_1,u_2}^{\mathrm{c,LoS/f/b}}\left(t,f\right)\right|^2\left(\tilde{\varphi}_{\mathrm{T},p_1}^{\mathrm{h}}-\mu_{\mathrm{T}}^{\mathrm{c,az,L/f/b}}\right)^2}{\sum_{p_1,p_2,u_1,u_2=1}^{P_{\mathrm{h}},P_{\mathrm{v}},Q_{\mathrm{h}}^{\mathrm{c}},Q_{\mathrm{v}}^{\mathrm{c}}}\left|h_{\mathrm{B},p_1,p_2,u_1,u_2}^{\mathrm{c,LoS/f/b}}\left(t,f\right)\right|^2}}. \tag{42}$$

The mean value of weighted azimuth beam for LoS/forward scattering/bi-directional scattering path can be calculated as

$$\mu_{\mathrm{T}}^{\mathrm{c,az,L/f/b}}=\frac{\sum_{p_1,p_2,u_1,u_2=1}^{P_{\mathrm{h}},P_{\mathrm{v}},Q_{\mathrm{h}}^{\mathrm{c}},Q_{\mathrm{v}}^{\mathrm{c}}}\left|h_{\mathrm{B},p_1,p_2,u_1,u_2}^{\mathrm{c,LoS/f/b}}\left(t,f\right)\right|^2\cdot\tilde{\varphi}_{\mathrm{T},p_1}^{\mathrm{h}}}{\sum_{p_1,p_2,u_1,u_2=1}^{P_{\mathrm{h}},P_{\mathrm{v}},Q_{\mathrm{h}}^{\mathrm{c}},Q_{\mathrm{v}}^{\mathrm{c}}}\left|h_{\mathrm{B},p_1,p_2,u_1,u_2}^{\mathrm{c,LoS/f/b}}\left(t,f\right)\right|^2}. \tag{43}$$

Furthermore, the RMS delay spread can be obtained as $\sigma_{\mathrm{B,DS}}^{\mathrm{c}}=\sigma_{\mathrm{B,DS}}^{\mathrm{c,L}}+\sigma_{\mathrm{B,DS}}^{\mathrm{c,f}}+\sigma_{\mathrm{B,DS}}^{\mathrm{c,b}}$. The LoS/forward scattering/bi-directional scattering components are acquired by substituting $\tilde{\varphi}_{\mathrm{T},p_1}^{\mathrm{h}}$ and $\mu_{\mathrm{T}}^{\mathrm{s,az}}$ to $\tau_{\mathrm{c},L/m_{n_1}/m_{n_0}}\left(t\right)$ and $\mu_{DS}^{\mathrm{s,L/f/b}}$ in (42) and (43), respectively.

### C. Temporal Doppler PSD

The temporal Doppler PSD reveals the distribution of channel power over the Doppler frequency shift, due to the movements of UE and (or) clusters. By performing the Fourier transform on the TACF of the sensing GBSM (BDCM), Doppler PSD of the sensing channel can be correspondingly obtained, i.e.,

$$\varpi_{(\mathrm{B})}^{\mathrm{s}}\left(\nu,t\right)=\int_{-\infty}^{+\infty}R_{(\mathrm{B}),p_1p_2q_1q_2}^{\mathrm{s}}\left(t,f,\Delta t\right)e^{-j2\pi\nu\Delta t}d\Delta t \tag{44}$$

where the subscript B means the Doppler PSD of BDCM. If the subscript B is removed, it means the Doppler PSD of GBSM. In addition, substituting $R_{(\mathrm{B}),p_1p_2u_1u_2}^{\mathrm{c}}\left(t,f,\Delta t\right)$ for $R_{(\mathrm{B}),p_1p_2q_1q_2}^{\mathrm{s}}\left(t,f,\Delta t\right)$, the Doppler PSD of the communication GBSM (BDCM) $\varpi_{(\mathrm{B})}^{\mathrm{c}}\left(\nu,t\right)$ can be obtained.

### D. Coherence Time

The coherence time characterizes the maximum time interval in the time domain during which the channel remains stationary. It is defined as the maximum time interval when TACF is greater than the specified threshold. We set the threshold for the sensing channel and the communication channel to be the same, i.e., $c_{\mathrm{th}}$. The coherence times of the sensing channel $C_{\mathrm{T}}^{\mathrm{s}}\left(t\right)$ and communication channel $C_{\mathrm{T}}^{\mathrm{c}}\left(t\right)$ can be expressed as

$$C_{\mathrm{T}}^{\mathrm{s}}\left(t\right)=\max\left\{\Delta t>0:R_{\mathrm{B},p_1p_2q_1q_2}^{\mathrm{s}}\left(t,f,\Delta t\right)=c_{\mathrm{th}}\right\} \tag{45}$$

$$C_{\mathrm{T}}^{\mathrm{c}}\left(t\right)=\max\left\{\Delta t>0:R_{\mathrm{B},p_1p_2u_1u_2}^{\mathrm{c}}\left(t,f,\Delta t\right)=c_{\mathrm{th}}\right\}. \tag{46}$$

### E. Channel Capacity

Channel capacity represents the maximum amount of information a channel can carry without errors and is an essential metric for communication system performance. Channel capacity is closely related to channel state information (CSI). The channel matrix includes the CSI required for channel capacity calculation, such as delay and angle parameters. Channel capacity, as a systematic evaluation, reflects the effectiveness of channel models in describing the propagation of signals in actual environments. In the downlink, the CSI can be obtained by UE using channel estimation or signal processing [55]. To focus more on the performance analysis of the channel model, we assume that the CSI is only known at UE. Then the channel capacity can be denoted as

$$Cap=E\left\{\log_2\det\left(\mathbf{I}+\frac{SNR}{P}\bar{\mathbf{H}}_{\mathrm{B}}^{\mathrm{c}}\left(t,f\right)\left[\bar{\mathbf{H}}_{\mathrm{B}}^{\mathrm{c}}\left(t,f\right)\right]^{\mathrm{H}}\right)\right\} \tag{47}$$

where $SNR$ is the signal-to-noise ratio (SNR), $\bar{\mathbf{H}}_{\mathrm{B}}^{\mathrm{c}}\left(t,f\right)=\mathbf{H}_{\mathrm{B}}^{\mathrm{c}}\left(t,f\right)\cdot\left[\frac{1}{PQ_{\mathrm{c}}}\|\mathbf{H}_{\mathrm{B}}^{\mathrm{c}}\left(t,f\right)\|_F\right]$ is the normalized communication channel matrix, and $\|\cdot\|_F$ is the second-order norm operation of a matrix.

## V. Results and Analysis

In this section, the simulation results of the statistical properties of the proposed ISAC channel model are investigated. Although there are shared clusters between sensing channel and communication channel, the differences in channel characteristics due to their different structures need to be studied. A detailed comparison of the statistical properties between the sensing channel and the communication channel is provided. In addition, the impact of converting from GBSM to BDCM on channel characteristics is also investigated by comparing the statistical properties of GBSM and BDCM. Furthermore, the feasibility and accuracy of the proposed channel model are verified by comparing simulation results and measurement results.

Figs. 4 (a) and (b) compare the TACFs of the sensing channel and communication channel in the beam domain and antenna domain, respectively. It can be seen that regardless of BDCM or GBSM, the attenuation speed of the TACF of the sensing channel is faster than that of the communication channel. This indicates that the sensing channel changes faster over time, and the movements of clusters and (or) UE exert a more remarkable influence on the sensing channel than the communication channel. This is because the sensing channel is composed of single-bounce sensing cluster echos, thus the movement of the cluster will cause a significant change in the sensing channel. Moreover, for both sensing and communication, the TACFs of BDCMs are greater than those of GBSMs for sensing and communication. It indicates that the channel in the beam domain has a stronger temporal correlation, and BDCM is more robust than GBSM in the time domain. Furthermore, the TACFs of sensing and communication channel models exhibit differences at $t$ = 0, 10, and 20 s, proving that the channel is non-stationary in the time domain.

Fig. 5 compares the SCCFs of sensing BDCM, communication BDCM, sensing GBSM, communication GBSM, and measurement data in [56]. The measurement was carried out in an outdoor scenario at 2.6 GHz with 128 element linear transmitting array. Comparing the SCCFs of BDCM and

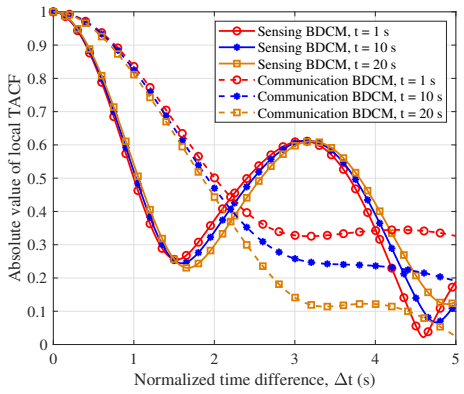


(a)

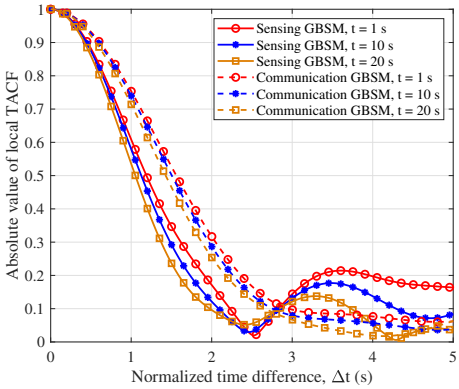


(b)

Fig. 4. Comparison of TACFs between (a) sensing BDCM and communication BDCM, and (b) sensing GBSM and communication GBSM at $t$ = 1, 10, and 20 s ($f_c$ = 2.6 GHz, $P_{\mathrm{h}}$ = 32, $P_{\mathrm{v}}$ = 32, $Q_{\mathrm{h}}^{\mathrm{s}}$ = $Q_{\mathrm{v}}^{\mathrm{s}}$ = $Q_{\mathrm{h}}^{\mathrm{c}}$ = $Q_{\mathrm{v}}^{\mathrm{c}}$ = 32, $d_{\mathrm{L}}(t)$ = 100 m, $v_{\mathrm{R}}(t)$ = 0 m/s, $L$ = 10, $K_l$ = 10, $N_1$ = $N_0$ = 5, $M_{n_1}$ = $M_{n_0}$ = 10, $v_{\mathrm{s},k_l}(t)$ = $v_{m_{n_1}}^{\mathrm{f}}(t)$ = $v_{m_{n_0}}^{\mathrm{b}}(t)$ = 1 m/s, $\alpha_{\mathrm{s},k_l}(t)$ = $\alpha_{m_{n_1}}^{\mathrm{f}}(t)$ = $\alpha_{m_{n_0}}^{\mathrm{b}}(t)$ = $\pi/3$).

GBSM, it can be found that the SCCFs of both sensing and communication BDCMs are greater than the corresponding SCCFs of sensing and communication GBSMs. The reason is that after the channel model is transformed from the antenna domain to the beam domain, the inter-beam power leakage results in an increase in the inter-beam correlation. As the beam spacing increases, the impact of power leakage gradually decreases, and the SCCFs in the beam domain and antenna domain become closer. At the same time, it can be observed that the SCCF of sensing BDCM is greater than that of communication BDCM. The reason is that, compared to the communication channel, there are more clusters in the sensing channel and their distribution range is wider, as shown in Fig. 2, which further aggravates the impact of beam power leakage. The SCCFs of sensing GBSM and communication GBSM exhibit a certain degree of similarity, for the reason that we set the same cluster distribution parameters. Finally, Fig. 5 shows a good agreement between the communication BDCM SCCF simulation result and measurement results, illustrating the validity of the channel model.

Figs. 6 (a) and (b) compare the FCFs of sensing and communication BDCMs, as well as the FCFs of sensing and communication GBSMs, respectively, when $f_c$ = 2.6, 11, and 28 GHz. It can be seen that the FCF of the sensing channel

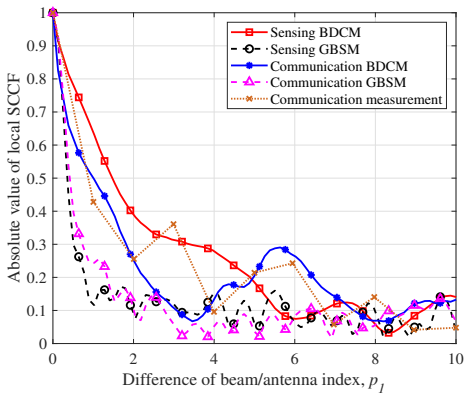


Fig. 5. Comparison of SCCFs of sensing BDCM, communication BDCM, sensing GBSM, communication GBSM and measurement data in [56] ($f_c$ = 2.6 GHz, $P_{\mathrm{h}}$ = 128, $P_{\mathrm{v}}$ = 1, $Q_{\mathrm{h}}^{\mathrm{s}}$ = $Q_{\mathrm{v}}^{\mathrm{s}}$ = $Q_{\mathrm{h}}^{\mathrm{c}}$ = $Q_{\mathrm{v}}^{\mathrm{c}}$ = 1, $p_2$ = $q_1$ = $q_2$ = $u_1$ = $u_2$ = 1, $d_{\mathrm{L}}(t)$ = 100 m, $L$ = 10, $K_l$ = 10, $N_1$ = $N_0$ = 5, $M_{n_1}$ = $M_{n_0}$ = 10, $v_{\mathrm{R}}(t)$ = $v_{\mathrm{s},k_l}(t)$ = $v_{m_{n_1}}^{\mathrm{f}}(t)$ = $v_{m_{n_0}}^{\mathrm{b}}(t)$ = 0 m/s ).

is greater than that of the communication channel both in the antenna domain and in the beam domain, due to the different structures of the sensing channel and communication channel. In addition, the FCF of BDCM is greater than that of GBSM for both sensing and communication. This indicates that power leakage increases the channel correlations in the frequency domain. Besides, the FCFs of sensing and communication exhibit differences at different carrier frequencies, demonstrating the frequency non-stationarity of sensing and communication channel models caused by the wideband of mmWave.

The RMS azimuth beam spreads of sensing BDCM, communication BDCM, and measurement data in [57] are compared in Fig. 7 when the $P_{\mathrm{h}}$ are 64 and 256. The measurement was conducted in a subway station scenario with $f_c$ = 11 GHz, $P_{\mathrm{h}}$ = 64, $P_{\mathrm{v}}$ = 4, and $Q_{\mathrm{h}}^{\mathrm{c}}$ = $Q_{\mathrm{v}}^{\mathrm{c}}$ = 1. In order to maintain the comparability between RMS azimuth beam spreads of the sensing channel and the communication channel, we set $Q_{\mathrm{h}}^{\mathrm{s}}$ = $Q_{\mathrm{v}}^{\mathrm{s}}$ = 1, which is the same as the Rx of the communication channel. It can be calculated that when $P_{\mathrm{h}}$ = 64 and 256, the mean values of RMS azimuth beam spreads of the sensing channel are $27.3973^\circ$ and $32.0519^\circ$, respectively. The mean values of RMS azimuth beam spreads of the communication channel are $33.1860^\circ$ and $34.5043^\circ$, respectively. The beam spread of the sensing channel is larger than that of the communication channel. This indicates that under the same parameter setting, the power distribution of the sensing channel is more even and dispersed than that of the communication channel, because the distribution of clusters varies, as shown in Fig. 2. At the same time, due to the power distributed more uniformly on beams of the sensing channel, the slope of the CDF curve of the sensing RMS azimuth beam spread is larger than that of the communication channel, which means the smaller variance of beam spread. The measurement results presented in Table IV of [40] are consistent with our simulation results. Furthermore, Fig. 7 shows that the more antennas there are, the greater the beam spread, which is caused by power leakage. Finally, the simulation result of RMS beam spread of the communication BDCM is found to be in coincidence with measurement results

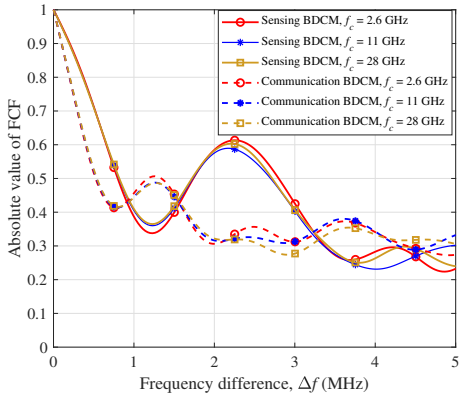


(a)

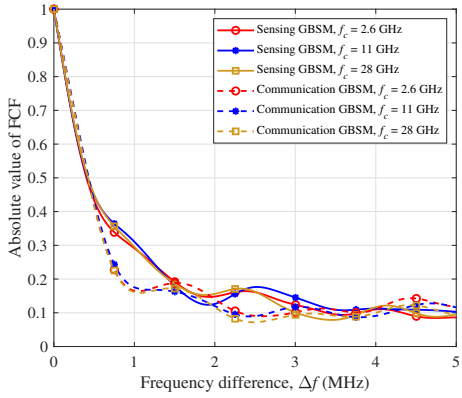


(b)

Fig. 6. Comparison of FCFs between (a) sensing BDCM and communication BDCM, and (b) sensing GBSM and communication GBSM at $f_c$ = 2.6, 11, and 28 GHz ($P_{\mathrm{h}}$ = 32, $P_{\mathrm{v}}$ = 32, $Q_{\mathrm{h}}^{\mathrm{s}} = Q_{\mathrm{v}}^{\mathrm{s}} = Q_{\mathrm{h}}^{\mathrm{c}} = Q_{\mathrm{v}}^{\mathrm{c}}$ = 32, $d_{\mathrm{L}}$ = 100 m, $v_{\mathrm{R}}(t)$ = 0 m/s, $L$ = 10, $K_l$ = 10, $N_1 = N_0$ = 5, $M_{n_1} = M_{n_0}$ = 10, $v_{\mathrm{s},k_l}(t) = v_{m_{n_1}}^{\mathrm{f}}(t) = v_{m_{n_0}}^{\mathrm{b}}(t)$ = 1 m/s, $\alpha_{\mathrm{s},k_l}(t) = \alpha_{m_{n_1}}^{\mathrm{f}}(t) = \alpha_{m_{n_0}}^{\mathrm{b}}(t) = \pi/3$).

[57], which illustrates the correctness of the channel model.

Fig. 8 compares RMS delay spreads of the sensing BDCM and the communication BDCM, and measurement results in [58]. The measurement was carried out at 5.3 GHz in an outdoor scenario, and the transmitting array is a $128 \times 8$ UPA. In order to fit the measurement data, we set $f_c$ = 5.3 GHz, $Q_{\mathrm{h}}^{\mathrm{s}} = Q_{\mathrm{v}}^{\mathrm{s}} = Q_{\mathrm{h}}^{\mathrm{c}} = Q_{\mathrm{v}}^{\mathrm{c}}$ = 2, and the transmitting array is set as $P_{\mathrm{h}} \times P_{\mathrm{v}} = 128 \times 8$ and $P_{\mathrm{h}} \times P_{\mathrm{v}} = 1024 \times 8$, respectively. As can be observed from Fig. 8, the RMS delay spread of the sensing BDCM is always larger than that of the communication BDCM, when the transmitting array is the same. This demonstrates that the power distribution in the sensing channel is more dispersed compared to the communication channel in the delay domain. Because the distribution of clusters of the sensing channel is more dispersed, while the distribution of clusters of the communication channel is more concentrated in the delay domain. The measurement results in Table IV of [40] made similar conclusions. Subsequently, the RMS delay spread simulation result of communication BDCM is well consistent with the measurement data in [58], which proves the correctness of the channel model. Finally, the RMS delay spread decreases with the increase in the number of antennas, whether it is the sensing channel or the communication channel. It is because the sparsity of the channel becomes notable

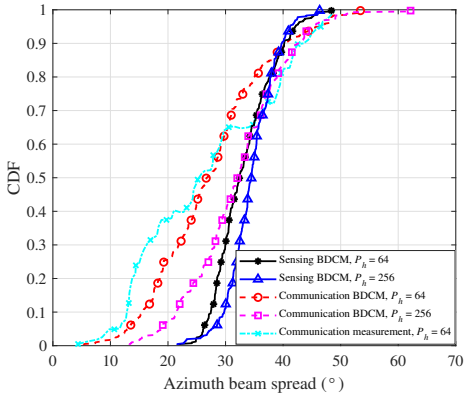


Fig. 7. Comparison of RMS azimuth beam spreads of sensing BDCM, communication BDCM, and measurement data in [57] ($f_c$ = 11 GHz, $P_{\mathrm{v}}$ = 4, $Q_{\mathrm{h}}^{\mathrm{s}} = Q_{\mathrm{v}}^{\mathrm{s}} = Q_{\mathrm{h}}^{\mathrm{c}} = Q_{\mathrm{v}}^{\mathrm{c}}$ = 1, $d_{\mathrm{L}}(t)$ = 100 m, $L$ = 10, $K_l$ = 10, $N_1 = N_0$ = 5, $M_{n_1} = M_{n_0}$ = 10, $v_{\mathrm{R}}(t)$ = 0 m/s, $v_{\mathrm{s},k_l}(t) = v_{m_{n_1}}^{\mathrm{f}}(t) = v_{m_{n_0}}^{\mathrm{b}}(t) = 0$ m/s).

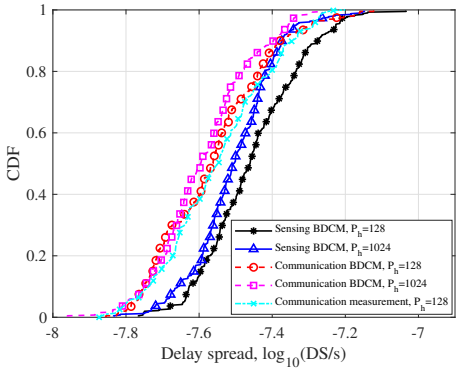


Fig. 8. Comparison of RMS delay spreads of sensing BDCM, communication BDCM, and measurement data in [58] ($f_c$ = 5.3 GHz, $P_{\mathrm{v}}$ = 8, $Q_{\mathrm{h}}^{\mathrm{s}} = Q_{\mathrm{v}}^{\mathrm{s}} = Q_{\mathrm{h}}^{\mathrm{c}} = Q_{\mathrm{v}}^{\mathrm{c}}$ = 2, $d_{\mathrm{L}}$ = 100 m, $v_{\mathrm{R}}(t)$ = 0 m/s, $L$ = 10, $K_l$ = 10, $N_1 = N_0$ = 5, $M_{n_1} = M_{n_0}$ = 10, $v_{\mathrm{s},k_l}(t) = v_{m_{n_1}}^{\mathrm{f}}(t) = v_{m_{n_0}}^{\mathrm{b}}(t)$ = 1 m/s, $\alpha_{\mathrm{s},k_l}(t) = \alpha_{m_{n_1}}^{\mathrm{f}}(t) = \alpha_{m_{n_0}}^{\mathrm{b}}(t) = \pi/3$).

as the number of antennas increases, and the distribution of power becomes sparse in the delay domain.

RMS Doppler spreads of BDCMs and GBSMs of sensing and communication with different transmitting and receiving UPAs are shown in Figs. 9 (a) and (b). In Fig. 9, it can be observed that the RMS Doppler spreads of sensing and communication BDCMs are smaller than that of GBSMs of them, respectively. This is because after converting from the antenna domain GBSM to the beam domain BDCM, the beam only contains clusters in the beam direction, so the multipath effect is not significant. In addition, the RMS Doppler spread of the sensing channel is always less than that of the communication channel. This indicates that the power dispersion of the sensing channel is more concentrated in the Doppler frequency shift than that of the communication channel. The reason is that the transmitting and receiving UPAs of the sensing channel are located at the same location, and the sensing channel only contains single-bounce clusters, thus further weakening the multipath effect. Furthermore, the RMS Doppler spread of the BDCM decreases significantly as the number of antennas increases. A potential cause for this

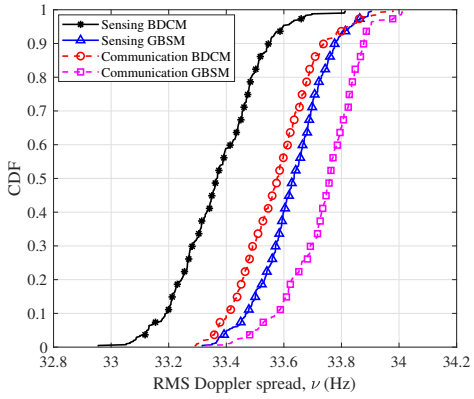


(a)

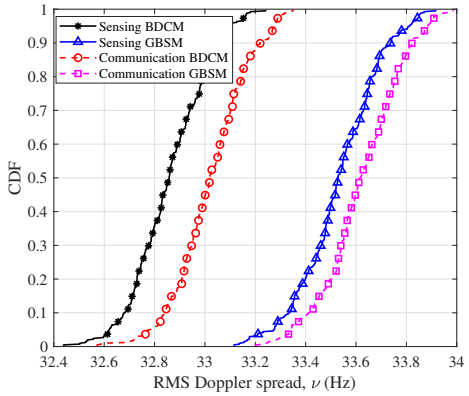


(b)

Fig. 9. RMS Doppler spreads of BDCMs and GBSMs of sensing and communication when (a) $P_{\mathrm{h}} = P_{\mathrm{v}} = Q_{\mathrm{h}}^{\mathrm{s}} = Q_{\mathrm{v}}^{\mathrm{s}} = Q_{\mathrm{h}}^{\mathrm{c}} = Q_{\mathrm{v}}^{\mathrm{c}} = 4$, and (b) $P_{\mathrm{h}} = P_{\mathrm{v}} = Q_{\mathrm{h}}^{\mathrm{s}} = Q_{\mathrm{v}}^{\mathrm{s}} = Q_{\mathrm{h}}^{\mathrm{c}} = Q_{\mathrm{v}}^{\mathrm{c}} = 32$ ($f_c = 28$ GHz, $v_{\mathrm{R}}(t) = 0$ m/s, $v_{\mathrm{s},k_l}(t) = v_{m_{n_1}}^{\mathrm{f}}(t) = v_{m_{n_0}}^{\mathrm{b}}(t) = 15$ m/s, $d_{\mathrm{L}} = 100$ m, $v_{\mathrm{R}}(t) = 0$ m/s, $L = 10$, $K_l = 10$, $N_1 = N_0 = 5$, $M_{n_1} = M_{n_0} = 10$, $v_{\mathrm{s},k_l}(t) = v_{m_{n_1}}^{\mathrm{f}}(t) = v_{m_{n_0}}^{\mathrm{b}}(t) = 1$ m/s, $\alpha_{\mathrm{s},k_l}(t) = \alpha_{m_{n_1}}^{\mathrm{f}}(t) = \alpha_{m_{n_0}}^{\mathrm{b}}(t) = \pi/3$).

result is that when the number of antennas increases, the beam width decreases and the power is concentrated, resulting in a decrease in the number of clusters in one beam and further weakening of multipath effects.

Fig. 10 shows the coherence time intervals of sensing BDCM and communication BDCM with different movement velocities of cluster. It can be observed that the coherence time interval of the sensing channel is always smaller than that of the communication BDCM when the speed of the cluster is the same. This indicates that under the same conditions, the sensing channel exhibits more significant time variety, which is resulted from the structure of the sensing single-bounce echo paths. Then, we can intuitively observe that as the speed of cluster movement increases, the coherence time interval decreases for both sensing and communication channels. This also indicates that, the faster the cluster moves, the larger the dynamic of the channel will be, resulting in a decrease in cluster stay time and larger beam dynamic [59]. Beam dynamic is an undeniable influencing factor in beamforming. Therefore, the motion of clusters and the coherence time interval of the channel are essential aspects that need to be considered in the beamforming research [60] of ISAC systems.

Fig. 11 depicts the channel capacity of the communication

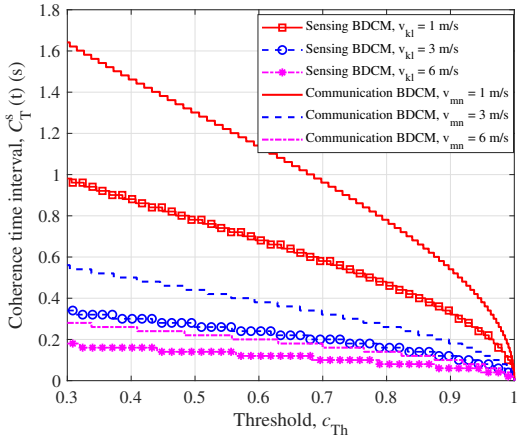


Fig. 10. Comparison of coherence time intervals of sensing BDCM and communication BDCM ($f_c = 28$ GHz, $P_{\mathrm{h}} = P_{\mathrm{v}} = 32$, $Q_{\mathrm{h}}^{\mathrm{s}} = Q_{\mathrm{v}}^{\mathrm{s}} = Q_{\mathrm{h}}^{\mathrm{c}} = Q_{\mathrm{v}}^{\mathrm{c}} = 32$, $d_{\mathrm{L}} = 100$ m, $v_{\mathrm{R}}(t) = 0$ m/s, $L = 10$, $K_l = 10$, $N_1 = N_0 = 5$, $M_{n_1} = M_{n_0} = 10$, $\alpha_{\mathrm{s},k_l}(t) = \alpha_{m_{n_1}}^{\mathrm{f}}(t) = \alpha_{m_{n_0}}^{\mathrm{b}}(t) = \pi/3$).

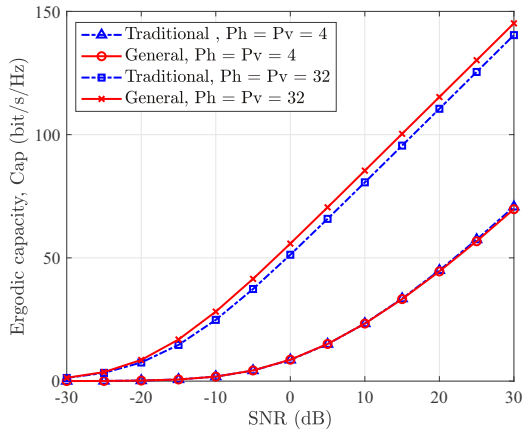


Fig. 11. Channel capacity of the communication BDCM with different UPAs ($f_c = 11$ GHz, $Q_{\mathrm{h}}^{\mathrm{s}} = Q_{\mathrm{v}}^{\mathrm{s}} = Q_{\mathrm{h}}^{\mathrm{c}} = Q_{\mathrm{v}}^{\mathrm{c}} = 4$, $d_{\mathrm{L}} = 100$ m, $v_{\mathrm{R}}(t) = 0$ m/s, $L = 10$, $K_l = 10$, $N_1 = N_0 = 5$, $M_{n_1} = M_{n_0} = 10$, $v_{\mathrm{s},k_l}(t) = v_{m_{n_1}}^{\mathrm{f}}(t) = v_{m_{n_0}}^{\mathrm{b}}(t) = 0$ m/s).

BDCM with different UPAs calculated by the traditional steering vector and the proposed general steering vector. It is evident from Fig. 11, when $P_{\mathrm{h}} \times P_{\mathrm{v}} = 4 \times 4$, the channel capacity calculated with the traditional steering vector is almost the same as the channel capacity calculated with the general steering vector proposed. However, when $P_{\mathrm{h}} \times P_{\mathrm{v}} = 32 \times 32$, the channel capacity calculated with the proposed general steering vector is significantly larger than the channel capacity calculated with the traditional steering vector. This shows that the proposed steering vector narrows the beamwidth and improves the communication channel capacity, proving the effectiveness of the proposed steering vector.

## VI. Conclusions

In this paper, novel 3D GBSM and BDCM for 6G mmWave massive MIMO ISAC systems have been proposed. The channel characteristics of the mmWave massive MIMO ISAC system have been considered in the channel model, including space-time-frequency non-stationarity, spherical wavefront, and shared clusters between sensing and communication

channels caused by the scattering characteristics. Under the same parameter settings, the shared first-bounce clusters have been observed, and the communication channel has exhibited more significant sparsity compared to the sensing channel. On the basis of the proposed channel model, the statistical properties of sensing BDCM, communication BDCM, sensing GBSM, and communication GBSM have been derived, simulated, and compared. The simulation results have illustrated that BDCM exhibits stronger correlations in space-time-frequency domains compared to GBSM. Moreover, the power distribution in the sensing channel is more dispersed than that in the communication channel in beam and delay domains, because the distribution of clusters of the sensing channel is more dispersed compared with the communication channel. The RMS Doppler spread results have demonstrated that the multipath effect weakens significantly after transitioning from GBSM to BDCM for sensing and communication channels. The sensing channel has exhibited more significant temporal non-stationarity than the communication channel, because the movement of clusters can have a significant impact on the sensing echo path. Furthermore, the proposed steering vector has narrowed the beamwidth of the beam by considering the spherical wavefront, thereby increasing channel capacity as the number of antennas increases. Finally, the good agreement between simulation results of statistical properties and measurement results has demonstrated the validity and effectiveness of the proposed channel model.

## REFERENCES


[1] C.-X. Wang, X. You, X. Gao, *et al*., "On the road to 6G: Visions, requirements, key technologies and testbeds," *IEEE Commun. Surveys Tuts.*, vol. 25, no. 2, pp. 905–974, 2nd Quart. 2023.

[2] C.-X. Wang, Z. Lv, X. Gao, *et al*., "Pervasive wireless channel modeling theory and applications to 6G GBSMs for all frequency bands and all scenarios," *IEEE Trans. Veh. Technol.*, vol. 71, no. 9, pp. 9159–9173, Sept. 2022.

[3] ITU-R, Draft New Recommendation, "Framework and overall objectives of the future development of IMT for 2030 and beyond," June 2023 [Online]. Available: https://www.itu.int/md/R19-SG05-C-0131

[4] F. Liu, C. Masouros, A. P. Petropulu, H. Griffiths, and L. Hanzo, "Joint radar and communication design: Applications, state-of-the-art, and the road ahead," *IEEE Trans. Commun.*, vol. 68, no. 6, pp. 3834–3862, June 2020.

[5] J. A. Zhang, F. Liu, C. Masouros, *et al.*, "An overview of signal processing techniques for joint communication and radar sensing," *IEEE J. Sel. Topics Signal Process.*, vol. 15, no. 6, pp. 1295–1315, Nov. 2021.

[6] N. H. Lehmann, A. M. Haimovich, R. S. Blum, and L. Cimini, "High resolution capabilities of MIMO radar", in *Proc. ACSSC'06*, Pacific Grove, CA, USA, Oct./Nov. 2006, pp. 25–30.

[7] A. Sakhnini, S. De Bast, M. Guenach, *et al.*, "Near-field coherent radar sensing using a massive MIMO communication testbed," *IEEE Trans. Wireless Commun.*, vol. 21, no. 8, pp. 6256–6270, Aug. 2022.

[8] T. K. Vu, C.-F. Liu, M. Bennis, *et al.*, "Ultra-reliable and low latency communication in mmWave-enabled massive MIMO networks," *IEEE Commun. Lett.*, vol. 21, no. 9, pp. 2041–2044, Sept. 2017.

[9] C.-X. Wang, J. Huang, H. Wang, *et al.*, "6G wireless channel measurements and models: Trends and challenges," *IEEE Veh. Technol. Mag.*, vol. 15, no. 4, pp. 22–32, Dec. 2020.

[10] S. M. Patole, M. Torlak, D. Wang, and M. Ali, "Automotive radars: A review of signal processing techniques", *IEEE Signal Process. Mag.*, vol. 34, no. 2, pp. 22–35, Mar. 2017.

[11] J. Choi, V. Va, N. Gonzalez-Prelcic, *et al.*, "Millimeter-wave vehicular communication to support massive automotive sensing", *IEEE Commun. Mag.*, vol. 54, no. 12, pp. 160–167, Dec. 2016.

[12] X. Liu, T. Huang, N. Shlezinger, *et al*., "Joint transmit beamforming for multiuser MIMO communications and MIMO radar," *IEEE Trans. Signal Process.*, vol. 68, pp. 3929–3944, June 2020.

[13] C. Qi, W. Ci, J. Zhang, and X. You, "Hybrid beamforming for millimeter wave MIMO integrated sensing and communications," *IEEE Commun. Lett.*, vol. 26, no. 5, pp. 1136–1140, May 2022.

[14] Z. Gao, Z. Wan, D. Zheng, *et al.*, "Integrated sensing and communication with mmWave massive MIMO: A compressed sampling perspective," *IEEE Trans. Wireless Commun.*, vol. 22, no. 3, pp. 1745–1762, Mar. 2023.

[15] J. A. Zhang, X. Huang, Y. J. Guo, J. Yuan, and R. W. Heath, "Multibeam for joint communication and radar sensing using steerable analog antenna arrays," *IEEE Trans. Veh. Technol.*, vol. 68, no. 1, pp. 671–685, Jan. 2019.

[16] A. Alkhateeb, J. Mo, N. Gonzalez-Prelcic, and R. W. Heath, "MIMO precoding and combining solutions for millimeter-wave systems," *IEEE Commun. Mag.*, vol. 52, no. 12, pp. 122–131, Dec. 2014.

[17] Y. Wu, F. Lemic, C. Han, and Z. Chen, "Sensing integrated DFT-spread OFDM waveform and deep learning-powered Rx design for terahertz integrated sensing and communication systems," *IEEE Trans. Commun.*, vol. 71, no. 1, pp. 595–610, Jan. 2023.

[18] Y. Li, Z. Wei, Z. Feng, *et al*., "Performance analysis of uplink joint sensing and communication system," in *Proc. IEEE/CIC ICCC'22*, Sanshui, Foshan, China, Aug. 2022, pp. 588–593.

[19] L. Liu, C. Oestges, J. Poutanen, *et al*., "The COST 2100 MIMO channel model", *IEEE Wireless Commun.*, vol. 19, no. 6, pp. 92–99, Dec. 2012.

[20] J. Flordelis, X. Li, O. Edfors, and F. Tufvesson, "Massive MIMO extensions to the COST 2100 channel model: Modeling and validation," *IEEE Trans. Wireless Commun.*, vol. 19, no. 1, pp. 380–394, Jan. 2020.

[21] X. Li, S. Zhou, E. Björnson, and J. Wang, "Capacity analysis for spatially non-wide sense stationary uplink massive MIMO systems," *IEEE Trans. Wireless Commun.*, vol. 14, no. 12, pp. 7044–7056, Dec. 2015.

[22] C. F. Lopez, C.-X. Wang, and Y. Zheng, "A 3D non-stationary wideband massive MIMO channel model based on ray-level evolution," *IEEE Trans. Commun.*, vol. 70, no. 1, pp. 621–634, Jan. 2022.

[23] J. Bian, C.-X. Wang, R. Feng, *et al*., "A novel 3D beam domain channel model for massive MIMO communication systems," *IEEE Trans. Wireless Commun.*, vol. 22, no. 3, pp. 1618–1632, Mar. 2023.

[24] Z. Huang, L. Bai, M. Sun, X. Cheng, P. E. Mogensen, and X. Cai, "A mixed-bouncing based non-stationarity and consistency 6G V2V channel model with continuously arbitrary trajectory," *IEEE Trans. Wireless Commun.*, vol. 23, no. 2, pp. 1634–1650, Feb. 2024.

[25] Y. Xie, B. Li, X. Zuo, M. Yang, and Z. Yan, "A 3D geometry-based stochastic model for 5G massive MIMO channels," in *Proc. QSHINE'15*, Taipei, 2015, pp. 216–222.

[26] Y. Zheng, C.-X. Wang, R. Yang, *et al*., "Ultra-massive MIMO channel measurements at 5.3 GHz and a general 6G channel model," *IEEE Trans. Veh. Technol.*, vol. 72, no. 1, pp. 20–34, Jan. 2023.

[27] L. Bai, Z. Huang, Y. Li and X. Cheng, "A 3D cluster-based channel model for 5G and beyond vehicle-to-vehicle massive MIMO channels," *IEEE Trans. Veh. Technol.*, vol. 70, no. 9, pp. 8401–8414, Sept. 2021.

[28] N. Ma, J. Chen, P. Zhang, and X. Yang, "Novel 3-D irregular-shaped model for massive MIMO V2V channels in street scattering environments," *IEEE Commun. Lett.*, vol. 9, no. 9, pp. 1437–1441, Sept. 2020.

[29] Z. Huang and X. Cheng, "A 3-D non-stationary model for beyond 5G and 6G vehicle-to-vehicle mmWave massive MIMO channels," *IEEE Trans. Intell. Transp. Syst.*, vol. 23, no. 7, pp. 8260–8276, July 2022.

[30] F. Lai, C.-X. Wang, J. Huang, X. Gao, and F.-C. Zheng, "A novel beam domain channel model for B5G massive MIMO wireless communication systems," *IEEE Trans. Veh. Technol.*, vol. 72, no. 4, pp. 4143–4156, Apr. 2023.

[31] Y. He, C.-X. Wang, H. Chang, *et al.*, "A novel 3-D beam domain channel model for maritime massive MIMO communication communication systems using uniform circular arrays," *IEEE Trans. Commun.*, vol. 71, no. 4, pp. 2487–2502, Apr. 2023.

[32] *Study on channel model for frequencies from 0.5 to 100 GHz (Release 18)*, document TR 38.901, V18.0.0, 3GPP, Apr. 2024.

[33] S. Ju, Y. Xing, O. Kanhere, and T. S. Rappaport, "Millimeter wave and sub-terahertz spatial statistical channel model for an indoor office building," *IEEE J. Sel. Areas Commun.*, vol. 39, no. 6, pp. 1561–1575, June 2021.

[34] Z. Ma, B. Ai, R. He, Z. Zhong, and M. Yang, "A non-stationary geometry-based MIMO channel model for millimeter-wave UAV networks," *IEEE J. Sel. Areas Commun.*, vol. 39, no. 10, pp. 2960–2974, Oct. 2021.

[35] B. Xiong, Z. Zhang, H. Jiang, *et al*., "A 3D non-stationary MIMO channel model for reconfigurable intelligent surface auxiliary UAV-to-ground mmWave communications," *IEEE Trans. Wireless Commun.*, vol. 21, no. 7, pp. 5658–5672, July 2022.

[36] Q. Zhu, K. Mao, M. Song, *et al*., "Map-based channel modeling and generation for U2V mmWave communication," *IEEE Trans. Veh. Technol.*, vol. 71, no. 8, pp. 8004–8015, Aug. 2022.

[37] H. Chang, C.-X. Wang, Y. Liu, *et al*., "A novel non-stationary 6G UAV-to-ground wireless channel model with 3D arbitrary trajectory changes," *IEEE Int. Things J.*, vol. 8, no. 12, pp. 9865–9877, June 2021.
[38] J. Xu, X. Cheng, and L. Bai, "A 3-D space-time-frequency non-stationary model for low-altitude UAV mmWave and massive MIMO aerial fading channels," *IEEE Trans. Antennas Propag.*, vol. 70, no. 11, pp. 10936–10950, Nov. 2022.
[39] A. Graff, A. Ali, and N. González-Prelcic, "Measuring radar and communication congruence at millimeter wave frequencies," in *Proc. ACSCC'19*, Pacific Grove, CA, USA, Nov. 2019, pp. 925–929.
[40] Y. Liu, J. Zhang, Y. Zhang, Z. Yuan, and G. Liu, "A shared cluster-based stochastic channel model for joint sensing and communication systems," arXiv:2211.06615, 2022.
[41] R. Yang, C.-X. Wang, J. Huang, E.-H. M. Aggoune, and Y. Hao, "A novel 6G ISAC channel model combining forward and backward scattering," *IEEE Trans. Wireless Commun.*, vol. 22, no. 11, pp. 8050–8065, Nov. 2023.
[42] Z. Zhang, R. He, B. Ai, *et al.*, "A general channel model for integrated sensing and communication scenarios," *IEEE Commun. Mag.*, vol. 61, no. 5, pp. 68–74, May 2023.
[43] S. Ju, S. H. A. Shah, M. A. Javed, *et al.*, "Scattering mechanisms and modeling for terahertz wireless communications," in *Proc. ICC'19*, Shanghai, China, May 2019, pp. 1–7.
[44] X. Li, J. He, Z. Yu, G. Wang, and P. Zhu, "Integrated sensing and communication in 6G: the deterministic channel models for THz imaging," in *Proc. PIMRC'21*, Helsinki, Finland, Sept. 2021, pp. 1–6.
[45] B. Antonescu, M. T. Moayyed, and S. Basagni, "Diffuse scattering models for mmWave V2X communications in urban scenarios," in *Proc. ICNC'19*, Honolulu, HI, USA, Feb. 2019, pp. 923–929.
[46] M. A. Richards, Fundamentals of Radar Signal Processing, New York, NY, USA: McGraw-Hill, 2014.
[47] J. Bian, C.-X. Wang, X. Gao, X. You, and M. Zhang, "A general 3D non-stationary wireless channel model for 5G and beyond," *IEEE Trans. Wireless Commun.*, vol. 39, no. 5, pp. 3211–3224, May 2021.
[48] S. Wu, C.-X. Wang, H. Aggoune, M. M. Alwakeel, and X.-H. You, "A general 3D non-stationary 5G wireless channel model," *IEEE Trans. Commun.*, vol. 66, no. 7, pp. 3065–3078, July 2018.
[49] C. Han, A. O. Bicen, and I. F. Akyildiz, "Multi-ray channel modeling and wideband characterization for wireless communications in the terahertz band," *IEEE Trans. Wireless Commun.*, vol. 14, no. 5, pp. 2402–2412, May 2015.
[50] J. Brady, N. Behdad, and A. Sayeed, "Beamspace MIMO for millimeter-wave communications: System architecture, modeling, analysis and measurements," *IEEE Trans. Antennas Propag.*, pp. 3814–3827, July 2013.
[51] A. M. Sayeed, "Deconstructing multiantenna fading channels," *IEEE Trans. Signal Process.*, vol. 50, no. 10, pp. 2563–2579, Oct. 2002.
[52] L. Huang, Y. Zhang, Q. Li, and J. Song, "Phased array radar-based channel modeling and sparse channel estimation for an integrated radar and communication system," *IEEE Access*, vol. 5, pp. 15468–15477, 2017.
[53] R. Feng, C.-X. Wang, J. Huang, and X. Gao, "Recent advances of ultramassive multiple-input, multiple-output technologies: Realizing a sixth-generation future in spatial and beam domains," *IEEE Veh. Technol. Mag.*, vol. 18, no. 1, pp. 70–79, Mar. 2023.
[54] C.-X. Wang, Z. Lv, Y. Chen, and H. Haas, "A complete study of space-time-frequency statistical properties of the 6G pervasive channel model," *IEEE Trans. Commun.*, vol. 71, no. 12, pp. 7273–7287, Dec. 2023.
[55] D. P. Palomar, J. R. Fonollosa, and M. A. Lagunas, "Capacity results of spatially correlated frequency-selective MIMO channels in UMTS," in *Proc. IEEE VTC-Fall'01*, Atlantic City, NJ, USA, 2001, pp. 553–557.
[56] S. Payami and F. Tufvesson, "Channel measurements and analysis for very large array systems at 2.6 GHz," in *Proc. EUCAP'12*, Prague, Czech, Mar. 2012, pp. 433–437.
[57] J. Li, B. Ai, R. He, M. Yang, Z. Zhong, and Y. Hao, "A cluster-based channel model for massive MIMO communications in indoor hotspot scenarios," *IEEE Trans. Wireless Commun.*, vol. 18, no. 8, pp. 3856–3870, Aug. 2019.
[58] Y. Zheng, C.-X. Wang, J. Huang, R. Feng, and J. Thompson, "Measurements and characteristics analysis of 6G ultra-massive MIMO wireless channels with different antenna configurations and scenarios," *IEEE Trans. Veh. Technol.*, vol. 72, no. 8, pp. 9720–9732, Aug. 2023.
[59] V. Raghavan, T. Bai, A. Sampath, O. H. Koymen, and J. Li, "Modeling and combating blockage in millimeter wave systems," in *Proc. SPAWC'18*, Kalamata, Greece, 2018, pp. 1–5.
[60] V. Raghavan, A. Partyka, L. Akhoondzadeh-Asl, M. A. Tassoudji, O. H. Koymen, and J. Sanelli, "Millimeter wave channel measurements and implications for PHY layer design," *IEEE Trans. Antennas Propag.*, vol. 65, no. 12, pp. 6521–6533, Dec. 2017.

**Runruo Yang** received the B.E. degree in Information and Communication Engineering from University of Electronic Science and Technology of China, in 2018. She is currently pursuing the Ph.D. degree in the National Mobile Communications Research Laboratory, Southeast University, China. Her research interests are massive MIMO wireless channel measurements and modeling, integrated sensing and communication channel measurements and modeling.

**Cheng-Xiang Wang** (Fellow, IEEE) received the B.Sc. and M.Eng. degrees in communication and information systems from Shandong University, Jinan, China, in 1997 and 2000, respectively, and the Ph.D. degree in wireless communications from Aalborg University, Aalborg, Denmark, in 2004.

He was a Research Assistant with the Hamburg University of Technology, Hamburg, Germany, from 2000 to 2001, a Visiting Researcher with Siemens AG Mobile Phones, Munich, Germany, in 2004, and a Research Fellow with the University of Agder, Grimstad, Norway, from 2001 to 2005. He was with Heriot-Watt University, Edinburgh, U.K., from 2005 to 2018, where he was promoted to a professor in 2011. He has been with Southeast University, Nanjing, China, as a professor since 2018, and he is now the Executive Dean of the School of Information Science and Engineering. He is also a professor with Pervasive Communication Research Center, Purple Mountain Laboratories, Nanjing, China. He has authored 4 books, 3 book chapters, and over 620 papers in refereed journals and conference proceedings, including 28 highly cited papers. He has also delivered 32 invited keynote speeches/talks and 21 tutorials in international conferences. His current research interests include wireless channel measurements and modeling, 6G wireless communication networks, and electromagnetic information theory.

Dr. Wang is a Member of the Academia Europaea (The Academy of Europe), a Member of the European Academy of Sciences and Arts (EASA), a Fellow of the Royal Society of Edinburgh (FRSE), IEEE, and IET, an IEEE Communications Society Distinguished Lecturer in 2019 and 2020, a Highly-Cited Researcher recognized by Clarivate Analytics in 2017-2020. He is currently an Executive Editorial Committee Member of the IEEE TRANSACTIONS ON WIRELESS COMMUNICATIONS. He has served as an Editor for over sixteen international journals, including the IEEE TRANSACTIONS ON WIRELESS COMMUNICATIONS, from 2007 to 2009, the IEEE TRANSACTIONS ON VEHICULAR TECHNOLOGY, from 2011 to 2017, and the IEEE TRANSACTIONS ON COMMUNICATIONS, from 2015 to 2017. He was a Guest Editor of the IEEE JOURNAL ON SELECTED AREAS IN COMMUNICATIONS, the IEEE TRANSACTIONS ON BIG DATA, and the IEEE TRANSACTIONS ON COGNITIVE COMMUNICATIONS AND NETWORKING. He has served as a TPC Chair and General Chair for more than 30 international conferences. He received IEEE Neal Shepherd Memorial Best Propagation Paper Award in 2024. He also received 19 Best Paper Awards from international conferences.

**Rui Feng** (Member, IEEE) received the B.Sc. degree in communication engineering, the M.Eng. degree in signal and information processing from Yantai University, Yantai, China, in 2011 and 2014, respectively, and the Ph.D. degree in communication and information System from Shandong University, Jinan, China, in 2018. From July 2018 to September 2020, she was a Lecturer with Ludong University, Yantai, China. She is currently a Postdoctoral Research Associate with Purple Mountain Laboratories and Southeast University, Nanjing, China. Her research interests include ultra massive MIMO channel modeling theory and beam domain channel modeling.

**Jie Huang** (Member, IEEE) received the B.E. degree in Information Engineering from Xidian University, China, in 2013, and the Ph.D. degree in Information and Communication Engineering from Shandong University, China, in 2018. From Oct. 2018 to Oct. 2020, he was a Postdoctoral Research Associate in the National Mobile Communications Research Laboratory, Southeast University, China, supported by the National Postdoctoral Program for Innovative Talents. From Jan. 2019 to Feb. 2020, he was a Postdoctoral Research Associate in Durham University, UK. Since Mar. 2019, he is a part-time researcher in Purple Mountain Laboratories, China. Since Nov. 2020, he is an Associate Professor in the National Mobile Communications Research Laboratory, Southeast University. He has authored and co-authored more than 120 papers in refereed journals and conference proceedings. He received IEEE Neal Shepherd Memorial Best Propagation Paper Award in 2024 and Best Paper Awards from WPMC 2016, WCSP 2020, WCSP 2021, and WCSP 2024. He has delivered over 10 tutorials in international conferences, including IEEE Globecom and IEEE ICC. His research interests include millimeter wave, massive MIMO, reconfigurable intelligent surface channel measurements and modeling, electromagnetic information theory, and 6G wireless communications.

**Yunfei Chen** (Senior Member, IEEE) received the B.E. and M.E. degrees in electronics engineering from Shanghai Jiaotong University, Shanghai, China, in 1998 and 2001, respectively, and the Ph.D. degree from the University of Alberta in 2006. He is currently working as a Professor with the Department of Engineering, University of Durham, U.K. His research interests include wireless communications, performance analysis, joint radar communications designs, cognitive radios, wireless relaying, and energy harvesting.

**El-Hadi M. Aggoune** (Life Senior Member, IEEE) received the M.S. and Ph.D. degrees in electrical engineering from the University of Washington (UW), Seattle, WA, USA, in 1984 and 1988, respectively. He is currently a Professor and the Director of the Sensor Networks and Cellular Systems (SNCS) Research Center, University of Tabuk, Tabuk, Saudi Arabia. He is listed as an inventor in several patents, one of them was assigned to Boeing Company, Chicago, IL, USA. He is a Professional Engineer registered in the state of Washington. He has coauthored articles in IEEE and other journals and conferences and served on editorial boards and technical committees for many of them. His research interests include wireless communication, sensor networks, power systems, neurocomputing, and scientific visualization. Dr. Aggoune received the IEEE Professor of the Year Award from UW. He was the Director of the laboratory that received the Boeing Supplier Excellence Award. He served at several universities in the USA and abroad at many academic ranks including endowed chair professor.